

The CLAS12 Ring Imaging Cherenkov Detector

M. Contalbrigo^a, V. Kubarovský^f, M. Mirazita^b, P. Rossi^{f,b}, G. Angelini^{b,j}, H. Avakian^f, K. Bailey^g, I. Balossino^a, L. Barion^a, F. Benmokhtar^h, P. Bonneau^f, W. Briscoeⁱ, W. Brooks^k, E. Cisbani^c, C. Cuevas^f, P. Degtiarenko^f, C. Dickover^f, K. Hafidi^g, K. Jooⁱ, A. Kimⁱ, T. Lemon^f, V. Lucherini^b, R. Malagutti^a, R. Montgomery^b, A. Movsisyan^a, P. Musico^d, T. O'Connor^g, D. Orecchini^b, L.L. Pappalardo^a, C. Pecar^h, R. Perrino^e, B. Raydo^f, S. Tomassini^b, M. Turisini^{a,b}, A. Yegneswaran^f

^aINFN Sezione di Ferrara and University of Ferrara, 44100 Ferrara, Italy

^bINFN Laboratori Nazionali di Frascati, 00044 Frascati, Italy

^cINFN Sezione di Roma1 - Gruppo Collegato Sanità and Italian National Institute of Health, 00153 Rome, Italy

^dINFN Sezione di Genova, 16146 Genova, Italy

^eINFN Sezione di Bari, 70126 Bari, Italy

^fThomas Jefferson National Accelerator Facility, Newport News, VA, 23606 USA

^gArgonne National Laboratory, Lemont, IL, 60439 USA

^hDuquesne University, Pittsburgh, PA, 15282 USA

ⁱUniversity of Connecticut, Storrs, CT, 06269 USA

^jThe George Washington University, Washington, DC, 20052 USA

^kUniversidad Técnica Federico Santa María, Casilla 110-V Valparaíso, Chile

Abstract

A ring imaging Cherenkov (RICH) detector has been installed in the CLAS12 spectrometer at Jefferson Laboratory (JLab) to provide kaon identification in the momentum range between 3 GeV/c and 8 GeV/c. The detector adopts a hybrid optics solution with aerogel radiator, light planar and spherical mirrors, and highly segmented photon detectors. We report here on the design, construction, and initial performance of the RICH during the commissioning of the detector and the first physics data taking period.

Keywords: Ring-imaging Cherenkov detectors, PID detectors, Single-photon detection

1. Overview

Particle identification (PID) of hadrons in the original baseline design of the Forward Detector of CLAS12 is obtained by combining the information from the High Threshold Cherenkov Counter (HTCC) [1], Low Threshold Cherenkov Counter (LTCC) [2], and Forward Time-of-Flight (FTOF) [3] systems. However, no sufficient separation of kaons from pions and protons can be achieved by using only these detectors in the momentum range relevant for the approved semi-inclusive deep inelastic scattering (SIDIS) physics program, i.e. between 3 GeV/c and 8 GeV/c. Therefore, improved particle identification in this momentum range is achieved by replacing two sectors of the existing LTCC with Ring Imaging Cherenkov (RICH) detectors. The first module of the RICH detector was completed before the start of the physics run, see Fig. 1, while the installation of the second module in the opposite sector is foreseen at the beginning of the CLAS12 operation with polarized targets. This article reports on the design, construction, and initial performance of the first RICH module. The second module will be identical to the first one.

The idea of a RICH detector is based on the fact that when a fast particle crosses a radiator with a velocity β larger than the velocity of the light in that medium, it generates Cherenkov radiation. The light is emitted in a cone with opening angle θ_C given by $\cos(\theta_C) = [\beta n(\lambda)]^{-1}$, where $n(\lambda)$ is the refractive index of the radiator, which may depend on the wavelength

λ . Following an expansion volume where the light cone opens up, the photons are detected and the RICH ring can be reconstructed. A precision measurement of the Cherenkov angle provides the determination of the particle velocity and, together with information from the tracking system, it allows its identification. Thus, the capability of identifying the particle types with a known momentum and different velocity is governed by the Cherenkov angle resolution, and it can be effectively parameterized by the separation in units of resolution n_σ between the angle distributions of the various particles.

2. The RICH Detector Requirements and Design

The CLAS12 spectrometer in Hall B [4] is designed to operate with highly polarized beams and nucleon targets at a luminosity of $10^{35} \text{ cm}^{-2}\text{s}^{-1}$. According to the SIDIS Monte Carlo studies, the kaon production rate is about one order of magnitude lower than the rates of pions and protons in most of the kinematic plane. Thus, successful kaon identification requires a rejection factor from pions around 1:500, i.e. a contamination in the kaon sample of a few percent. This corresponds to 4σ separation. In the momentum range between 3 GeV/c and 8 GeV/c, neither gas nor liquid radiators provide sufficient angular separation to achieve the required pion rejection factor (see Fig. 2) and the only viable solution is the use of silica aerogel as radiator. Aerogel is an amorphous solid



Figure 1: The first module of the CLAS12 RICH installed in Sector 4 of the Hall B Forward Carriage.

52 network of SiO_2 nanocrystals with a very low macroscopic
53 density and a refractive index in between gases and liquids.

54 To detect the Cherenkov light emitted in the visible wave-
55 length range, Hamamatsu multi-anode photomultiplier tubes
56 (MaPMTs) were chosen for their high quantum efficiency
57 in the visible and near ultraviolet (UV) regions, their fast
58 response, and the required spatial resolution. Since the RICH
59 detector must fit into the original CLAS12 Forward Carriage,
60 there were several constraints imposed upon its design. Each
61 sector requires a projective geometry, limited depth of 1.2 m,
62 and $\sim 4.5 \text{ m}^2$ entrance windows. Simulation studies favored
63 a hybrid imaging Cherenkov detector design incorporating
64 aerogel radiators, visible light photon detectors, and a focusing
65 mirror system. The focusing mirror system is used to reduce the
66 detection area instrumented by the photon detectors to $\sim 1 \text{ m}^2$
67 per sector, minimizing costs and influence on the downstream
68 FTOF and Electromagnetic Calorimeter [5] systems. Depending
69 upon the incident particle track polar angle, Cherenkov
70 light is either imaged directly or after one or more reflections
71 and passes through the aerogel. Figure 3 shows a schematic
72 view of two examples of direct imaging and imaging after
73 multiple reflections. Such a peculiar hybrid-optics design is an
74 innovative solution that has been successfully validated with a
75 test-beam campaign [6].

76 The RICH detector replaces two sectors of the existing gas
77 Low Threshold Cherenkov detector (LTCC), which is located at
78 a 5-m distance from the beam-target interaction point. The first
79 RICH module was designed while the CLAS12 spectrometer
80 was already under construction and, as a consequence, it had to
81 cover the same large area to match the trapezoidal shape of the
82 LTCC sector. This resulted in several challenging requirements
83 for the mechanical structure. The guiding principles are to
84 minimize the material budget inside the acceptance and to
85 limit the impact on the downstream detectors, ensuring at

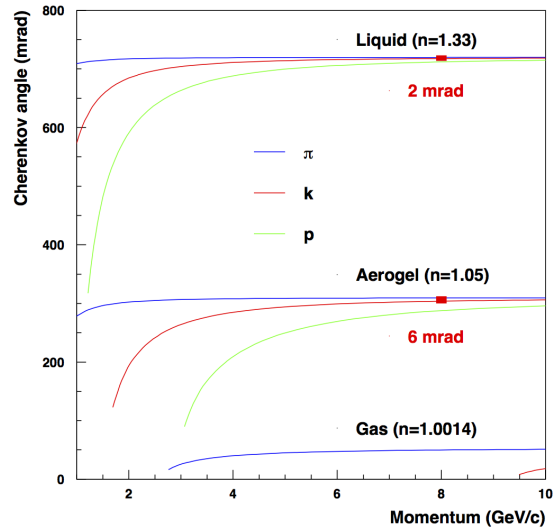


Figure 2: Cherenkov light opening angle as a function of the momentum for different particles using liquid, gas, or aerogel radiators. The angular separation between kaons and pions at the highest momenta is also indicated.

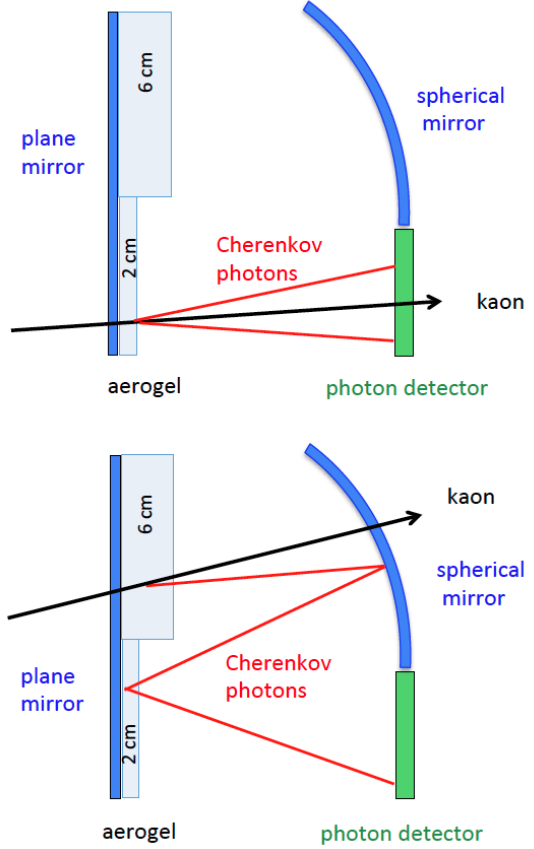


Figure 3: Examples of CLAS12 RICH imaging: direct detection of the Cherenkov cone produced in the thin aerogel layer (top plot); detection of the Cherenkov cone produced in the thick aerogel layer after multiple reflections and passes through the thin aerogel layer (bottom plot). The plot is not to scale.

the same time the rigidity of the structure imposed by the optical requirements. Therefore, light materials, in particular carbon fiber, are chosen for the most of the elements inside the CLAS12 acceptance. For all the parts with large dimensions, the sandwich technique, in which two thin solid skins are glued together on a thick honeycomb core, was also used. This technique indeed combines high stiffness with substantial weight reduction, resulting in a total weight of the detector of about 900 kg, ~30% lower than the LTCC.

A sketch of the detector is shown in Fig. 4. It is composed of a trapezoidal box (larger base of 4.2 m, smaller base of 0.3 m, height of 3.7 m, and depth of 1.2 m) in which all of the active elements are installed: the wall of aerogel tiles, the mirrors, the photomultiplier tubes (PMTs), and the electronics. The main structural elements of the box are: the two lateral panels made of aluminum sandwich, the top panel made of carbon-fiber sandwich, and the two upper angular elements and the bottom element made of aluminum. Each of the lateral panels supports two planar mirrors, while another planar mirror is installed on the bottom of the box. The box is closed on the front face (with respect to the beam direction) by two entrance panels made of a sandwich of two 1-mm-thick carbon-fiber skins glued on a Nomex honeycomb core. Two planar mirrors with a wall of 2-cm-thick aerogel tiles are installed on the lower entrance panel, while a wall made of two layers of 3-cm-thick aerogel tiles is installed on the upper one. Therefore, the profile of the entrance panels was specifically designed not only to ensure the best light and gas tightness, but also to include stiffening ribs for the installation of the mirrors and the aerogel. The same sandwich structure was used for the electronics panel, located on the bottom part of the backward face of the box. It is composed of a main panel where all of the front-end electronics and the PMTs are installed, and a thin cover. The panel and the cover are screwed together on the mechanical structure, making a very rigid system. Finally, a very light exit panel made of a thin Tedlar sheet glued on an aluminum frame not supporting any active element, closes the back face of the trapezoidal box.

The total material budget of the detector is largely dominated by the electronics panel, which contributes to approximately $0.3X_0$ in the region from the beamline up to about 17° . A sizable contribution comes also from the aerogel (with a maximum contribution of $0.05X_0$ in the polar angles from 17° to 26°), while other active components like the spherical and planar mirrors contribute only $\approx 0.01X_0$ each. The total material budget of the passive elements is estimated to be, on average, below $0.05X_0$.

The mechanical structures and all of the active elements (mirrors, aerogel, electronics, MaPMTs) define the RICH detector. The RICH is attached to the CLAS12 Forward Carriage by means of steel connections, attached to the angular and bottom elements. Detailed Finite Element Analysis (FEA) studies were performed in order to optimize the design of the detector with respect to the maximum deformation allowed by the required accuracy of the optical systems. These studies included optimization of the ratio between the skin and honeycomb thicknesses of the sandwich, and of the total thickness and profile of various stiffening and connection elements.

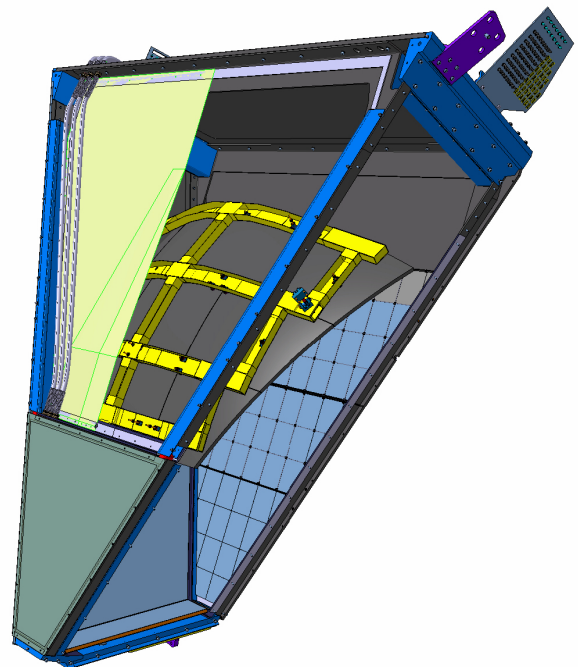


Figure 4: A schematic drawing of the CLAS12 RICH (rear view) with the internal components highlighted. From left to right, the components of the upper half are exit panel, spherical mirror support and sub-mirrors, double 3-cm-thick aerogel layer, and entrance panel. The components of the lower half are cover, electronics panel - mounting the front-end readout and the MaPMT sensors, 2-cm-thick aerogel layer, front planar mirrors, and entrance panel.

Simulations of the load conditions during the assembly and installation of the detector and in the RICH final position in CLAS12 were also performed together with a seismic analysis¹. These simulations demonstrated that all stresses produced on the detector elements during the installation are well within the elastic regime, and that the total deformations expected when the RICH is installed in CLAS12 never exceed a few millimeters.

3. The RICH Detector Components

3.1. The Aerogel Radiator

The aerogel radiator was produced by the *Budker and Boreskov Institute of Nuclear Physics* (Russia), which was able to fabricate tiles of different shapes and thicknesses, a critical requirement of the complex CLAS12 geometry. A total of 102 tiles with nominal refractive index 1.05, cut into squares $200 \times 200 \text{ mm}^2$, as well as pentagonal, trapezoidal, and triangular shapes, were assembled in two sections. The first section, covering the region between the beam pipe and the polar angle of 17.5° , was made of one layer of 2-cm-thick tiles. The second section, covering the polar angles between 17.5°

¹According to US regulations, seismic analyses are performed by increasing the expected weight load by 10%.

163 and 26° , was made of two layers of 3-cm-thick tiles, the largest
 164 aerogel tiles ever used in Cherenkov imaging applications at
 165 this high value of refractive index.

166 Each tile was tested to determine the geometric and optical
 167 parameters [7]. The measured geometric parameters are the
 168 side length and thickness, and the planarity of the tile surface.
 169 The measured optical parameters include the refractive index at
 170 the reference wavelength of 400 nm, and the light transmission
 171 as a function of the wavelength. The transparency parameter
 172 A_0 , the clarity parameter C , and the scattering length L_{scatt} at
 173 400 nm are then extracted from the measured optical properties
 174 using the Hunt parameterization [8]. Distributions of the
 175 measured values of the refractive index, transparency A_0 (in
 176 percent), and scattering length L_{scatt} for the square 2 cm
 177 tiles are shown in Fig. 5. The average values obtained over
 178 all of the 2 cm tiles are $L_{scatt} = 50.5$ mm, $A_0 = 0.975$,
 179 and $C = 0.00512 \mu\text{m}^4/\text{cm}$. The 3cm tiles feature similar
 180 optical quality [7]. From these measurements, the expected
 181 photon yield for $\beta = 1$ particles is estimated to be about 19
 182 photoelectrons (p.e.) in the 2 cm sector and about 25 in the
 183 6 cm (3 cm + 3 cm) sector.

184 3.2. The Mirror System

185 The mirror system, composed of planar and spherical mirrors,
 186 was designed to minimize the photon loss and to direct
 187 as much of the Cherenkov radiation as possible toward the
 188 photodetectors. Simulations were performed to optimize the
 189 segmentation, the position, and the radius of curvature of
 190 these mirrors, and to define the specifications of the optical
 191 performance. A drawing of the system is shown in Fig. 6.

192 3.2.1. The Spherical Mirrors

193 The spherical mirror system, installed inside the RICH box
 194 in front of the exit panel, has a total surface of about 3.6 m^2 ,
 195 a radius of curvature $R = 2.7 \text{ m}$, and is segmented into 10
 196 sub-mirrors. They were produced by the *Composite Mirror*
 197 *Applications* company [9], and are made of two layers of
 198 carbon fiber glued on a honeycomb core of small carbon-fiber
 199 cylinders. The areal weight of these mirrors is less than
 200 5 kg/m^2 , with an improvement of about 20% with respect
 201 to the mirrors produced by the same company for the LHCb
 202 experiment [10]. Each mirror is positioned on a light carbon
 203 frame by means of three special joints equipped with a spring
 204 and a precision screw that allowed their relative alignment. The
 205 frame is then attached to the mechanical structure by means of
 206 three similar joints that allow the alignment of the full mirror
 207 system with respect to the other active elements of the detector.

208 The accuracy of the spherical surface of the sub-mirrors was
 209 quantified by means of a so-called spot size measurement, in
 210 which each mirror was illuminated with a point-like light source,
 211 and the size of the reflected spot was measured by a XIMEA
 212 camera with a 1-cm-wide CMOS sensor. The size of the spot
 213 is quantified by D_0 , which is defined as the minimum diameter
 214 containing 90% of the total reflected light, and is related to the
 215 angular resolution of the reflected photons by the relation

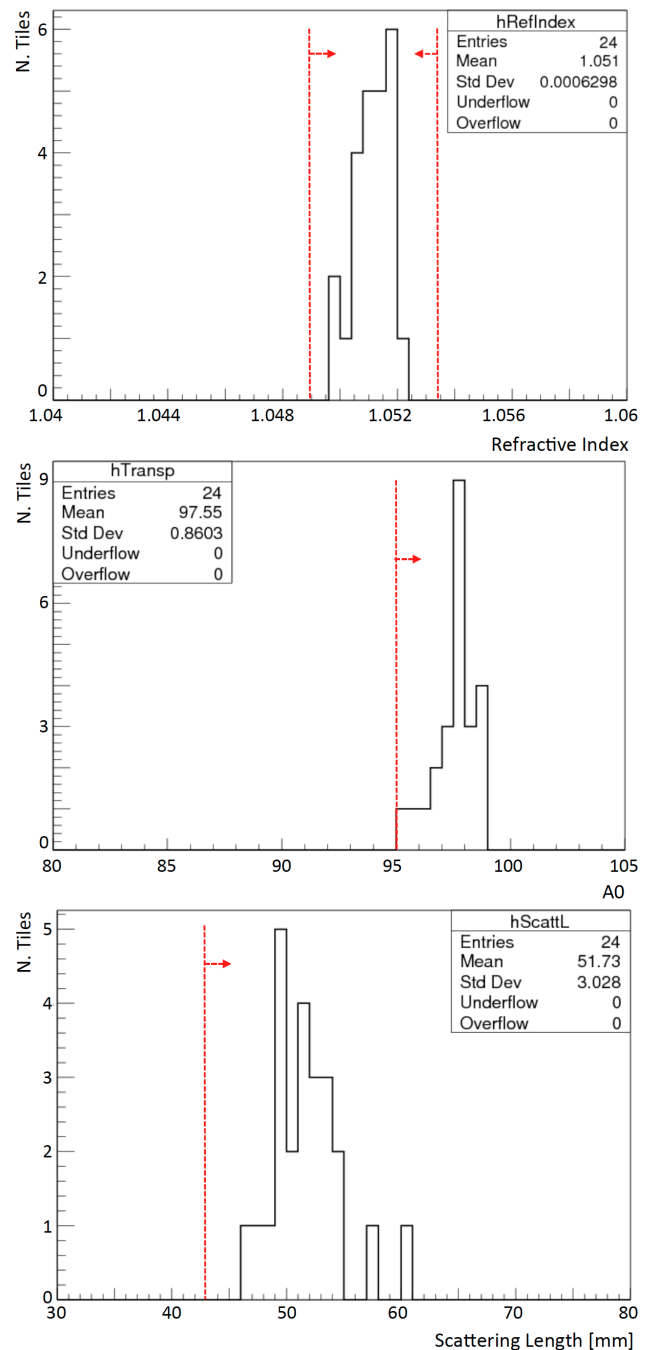


Figure 5: Distributions of the measured refractive index (top plot), transparency A_0 (in percent, central plot), and scattering length L_{scatt} (bottom plot) for the square 2 cm tiles. The red dashed lines indicate the specification limits.

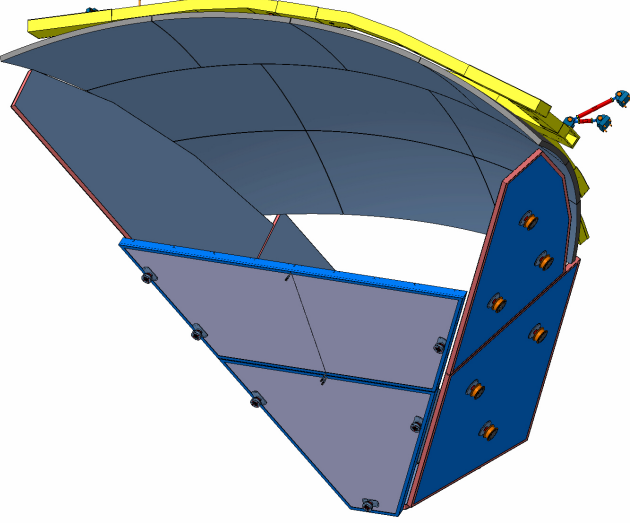


Figure 6: Drawing of the CLAS12 RICH mirror system with their mounting joints (front view). The 10 sub-mirrors of the spherical mirror face the two front planar mirrors. An array of planar mirrors, two on each side and one (not visible) on the bottom, completes the light-containment system.

$$\sigma_\theta = \frac{D_0}{8R}, \quad (1)$$

where the angular dispersion is derived from the 2σ -spot radius $D_0/2$ divided by the traveled distance $2R$ [11]. The smaller D_0 is, the closer the mirror surface is to a perfect sphere. The measurements also allow for the extraction of the radius of curvature, which corresponds to the distance between the camera and the mirror where the spot size is minimal. The results of a typical measurement of one sub-mirror are shown in Fig. 7, where D_0 as a function of the distance and the shape of the spot at the beginning of the distance scan and at the minimum are shown. All of the sub-mirrors exhibit a D_0 smaller than 1.5 mm, which means σ_θ significantly below 1 mrad, and a variation in the measured radii below 0.5%. All of these numbers are well within the specifications.

The sub-mirrors were coated with a reflecting layer by *Evaporated Coatings Inc* [12]. The quality of this coating was verified by measuring the reflectivity on several surface spots in the wavelength range from 300 to 650 nm. For all of the sub-mirrors, we obtained on average a reflectivity between 88% and 90%, relatively flat over the whole wavelength range.

3.2.2. The Planar Mirrors

The planar mirror system is composed of 7 mirrors: two installed on each of the lateral panels, two on the front panel, and one on the bottom, for a total surface area of about 6.5 m^2 . These mirrors were produced by the *Media Lario* company [13] and are made of two thin layers of glass glued on an aluminum honeycomb core. This is a standard technique widely used in telescopes for astrophysics studies but used for the first time in nuclear physics experiments, and allows for the production

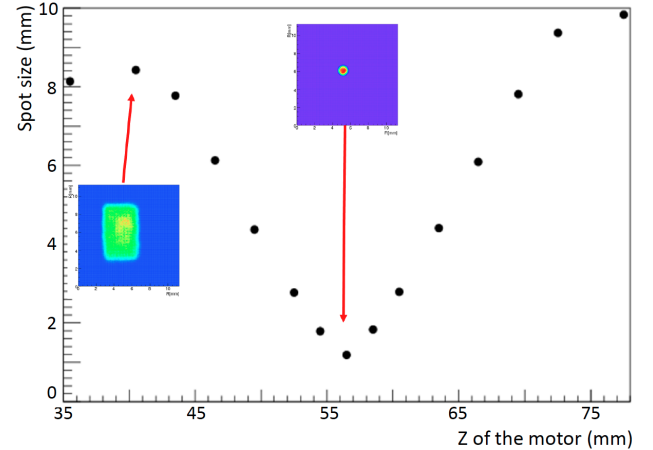


Figure 7: D_0 as function of the distance between the mirror and the camera for one of the spherical sub-mirrors. The two inserts show the shape of the reflected spot at the beginning of the distance scan and at the minimum.

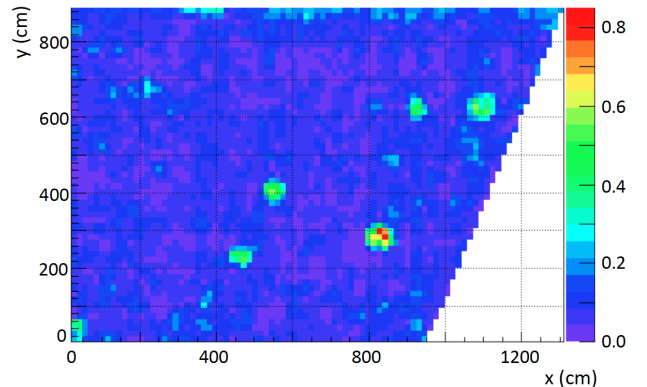


Figure 8: Profile of the local slope (indicated by the color scale in mrad) of the surface of one of the lateral planar mirror measured with a CMM.

of mirrors as light as the carbon fiber ones but at much lower cost. Being in the acceptance of the detector, the front mirrors use very thin (0.7 mm) glass layers, allowing a reduction of the material budget down to about $0.01X_0$, while for the lateral and the bottom mirrors, thicker (1.6 mm) glass layers were used.

The planarity of the mirror was measured with a Coordinate Measuring Machine (CMM). Typically, the measured accuracy of the surface was a few microns RMS. To better quantify the quality of the surface, the local slope profile was reconstructed from the spatial profile, as shown for one of the lateral mirrors in Fig. 8, where we see only a few spots with non-zero slope over a largely flat surface. All of the mirrors satisfy the requirement that only a few percent of the total surface should exceed a local slope of 0.3 mrad.

The characterization of the planar mirrors was completed by measuring the reflectivity in a few random spots of the surface in the wavelength range from 300 to 650 nm. The measurements showed a maximum reflectivity of approximately 95% at 400 nm and a reflectivity higher than 90% in the whole range.

263 **3.3. The Photon Detector**

264 Thanks to the use of mirrors, the active area is minimized
 265 to about 1 m^2 . The instrumented area is optimized to cover
 266 the most effective region close to the beam pipe, which is
 267 where the density of particles per unit area is the highest, the
 268 particle momenta are to a large extent above the FTOF working
 269 range, and the hadron identification requires the best RICH
 270 performance.

271 **3.3.1. The Photosensor**

272 Due to the imaging aspects of the RICH, there are several
 273 requirements that the photon sensor has to fulfill: it has to
 274 efficiently detect single photoelectron (SPE) level signals, it
 275 must be sensitive in the visible light wavelengths (due to the
 276 aerogel radiator material), it must have the spatial resolution
 277 required to achieve the design angular resolution, and it has to
 278 provide an active area with minimal dead space. In addition,
 279 it has to be insensitive to the low torus fringe field where the
 280 RICH readout is located, which is estimated to be no more than
 281 3.5 G, see Fig. 9. The Hamamatsu flat-panel H8500 MaPMT
 282 [14] with an 8×8 array of $6 \times 6 \text{ mm}^2$ pixels over a compact active
 283 area of $5 \times 5 \text{ cm}^2$ and with high packing fractions (89%), was
 284 initially selected as a good candidate. Despite not advertised as³¹⁷
 285 the optimal choice in the SPE regime, such MaPMTs showed³¹⁸
 286 adequate performance in several laboratory tests [15] and beam³¹⁹
 287 tests [16]. Just after the RICH construction startup, a novel
 288 Hamamatsu H12700 MaPMT became available, with the same³²⁰
 289 layout as the H8500 MaPMT, but an optimized dynode structure³²¹
 290 for single photon detection [17].

291 Of the 391 MaPMTs that the CLAS12 RICH employs, 80³²³
 292 are of the H8500 type and the rest are of the H12700 type.³²⁴
 293 This results in a total of 25024 individual pixels, covering³²⁵
 294 the $\sim 1 \text{ m}^2$ trapezoidal active area of the first RICH module.³²⁶
 295 The production specifications included requirements on the³²⁷
 296 minimum gain of 1×10^6 and a maximum total dark current³²⁸
 297 of 5 nA. Both were fully achieved. Figure 10 shows the³²⁹
 298 distribution of the pixel gains, which has an average value of³³⁰
 299 2.7×10^6 , corresponding to about 430 fC generated charge per³³¹
 300 SPE.

301 **3.3.2. The Readout Electronics**

302 The RICH front-end electronics are designed to ensure 100%³³⁶
 303 efficiency at 1/3 of the average photoelectron signal level, 1 to 4³³⁷
 304 gain spread compensation, time resolution of the order of 1 ns³³⁸
 305 to distinguish direct from reflected photon hits, and a trigger³³⁹
 306 rate up to 20 kHz with 8 μs trigger latency and negligible dead³⁴⁰
 307 time [18].

308 The front-end electronics are organized into compact units³⁴¹
 309 (called tiles, see Fig. 11) mechanically designed to fit the³⁴²
 310 MaPMT dimensions, each serving two or three MaPMTs, thus³⁴³
 311 allowing the tessellation of large surfaces with minimum dead³⁴⁴
 312 space and material budget. Each readout unit comprises three³⁴⁵
 313 boards with complementary functions.

314 A feed-through adapter board provides the electrical connec-³⁴⁷
 315 tivity of the sensors with the external readout system, while³⁴⁸
 316 preserving the adequate light and gas tightness of the inner³⁴⁹

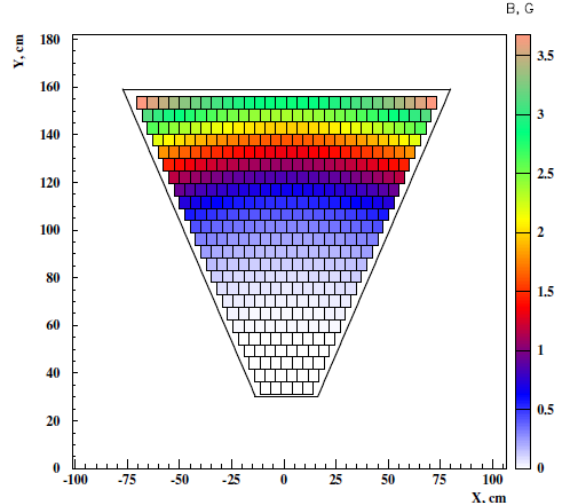


Figure 9: Calculated map of the torus fringe field strength (in Gauss) in the RICH photodetector area.

detector volume when mounted on the RICH carbon-fiber supporting panel. It also distributes the sensor bias voltage (with -1000 V as the nominal value).

The signal processing board is based on the MAROC3 chip [19], a 64-channel microcircuit dedicated to MaPMT pulse processing. Each channel comprises a low impedance adjustable gain preamplifier followed by two highly configurable shaping sections with independent processing. The first section embeds a slow shaper and a sample-and-hold structure to allow linear charge measurements up to 5 pC. Requiring short trigger delays and multiplexed access, this section can be used as a RICH calibration tool. The second section features a fast shaper and an adjustable threshold discriminator to produce, for each input signal, a start and stop logic pulse. A constant-threshold binary readout requires good stability of the baseline (pedestal) and definition of the working point (gain and threshold). During the board production, quality assurance tests confirmed the excellent sensitivity of the logic readout, able to discriminate signals down to a few percent of a single photoelectron discharge, as will be extensively discussed in Section 4.2.

The third stage of the readout is made of the FPGA boards, hosting a Xilinx7 FPGA chip, responsible for configuring and reading the front-end MAROC3, distributing the trigger, and interfacing with the data acquisition system [20] via optical link. The FPGA provides a TDC functionality with a 1 ns time stamp for both start and stop times. The start time is used for timing purposes, while the difference between the stop and start times, the so-called Time-Over-Threshold (ToT), provides a non-linear estimate of the amplitude of the input signal and is used for the time-walk correction, see Section 5.2. Finally, the FPGAs also embed a scaler readout that is used as a calibration and monitoring tool.

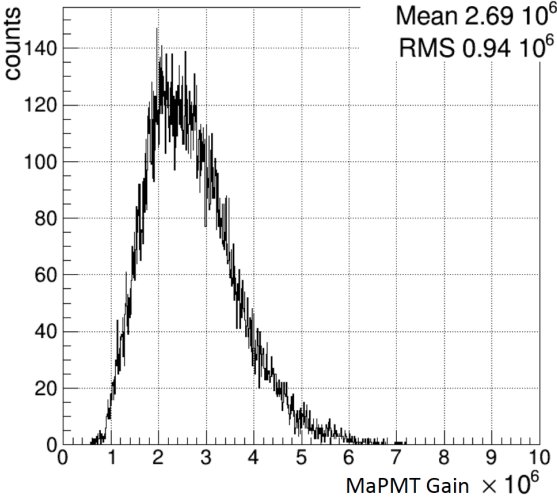


Figure 10: Distribution of the data-sheet gains of the 25k RICH MaPMT channels.

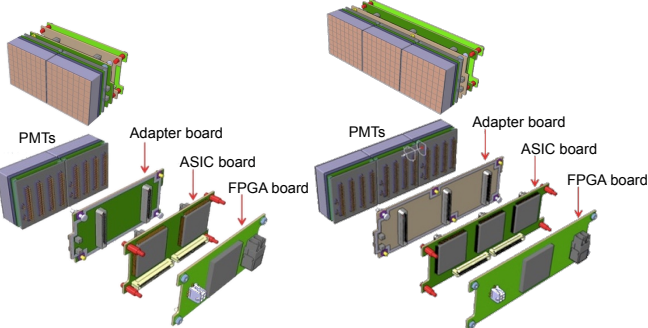


Figure 11: The CLAS12 RICH readout unit design (see text for details).

3.3.3. MaPMT Characterization

The characterization of hundreds of MaPMTs is a challenging problem. In order to test them efficiently within a reasonable time frame, a fully automated test stand was built to evaluate 6 MaPMTs at once. The test stand consists of a 470 nm diode laser system, 2 long-travel motorized stands to drive a laser fiber in two-dimensional space for individual pixel illumination, and a motorized neutral-density filter system. The laser light is directed through the fiber and attenuated to the single-photon level using neutral-density filters to mimic the conditions of the RICH detector. The motors are remotely controlled to move the focused laser 1 mm beam spot across the entire surface of the MaPMT entrance window and illuminate one by one the 64 pixels individually (see Fig. 12a). Alternatively, one can illuminate the whole surface of the MaPMT photocathode at once using an Engineered Diffuser to produce a square pattern with a non-Gaussian intensity distribution (see Fig. 12b). The latter configuration was used for the massive characterization of the RICH MaPMTs, bringing routine workloads to a minimum. The evaluation of 6 MaPMTs (corresponding to 384 individual channels) at 4 different high

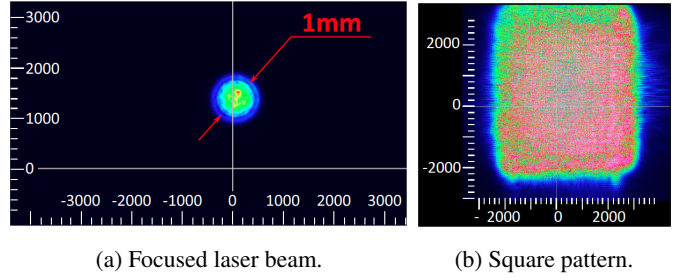


Figure 12: The MaPMT test stand laser output options. The images are taken at an arbitrary distance from the source, the scale is in micron.

voltages and 6 different light intensities was completed in 6 hours with less than 15 minutes of human intervention.

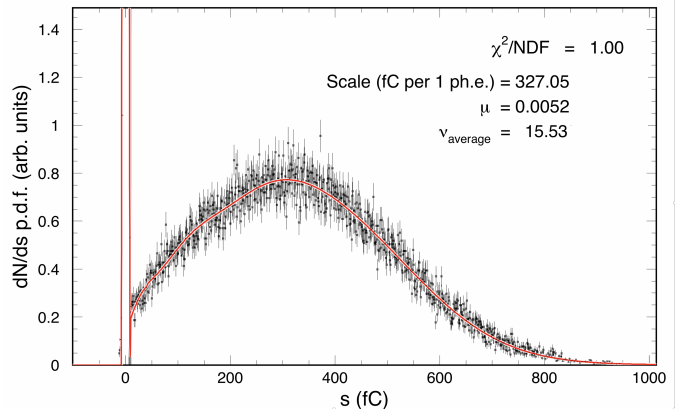


Figure 13: Sampled H8500 MaPMT single photoelectron spectrum from one of the pixels at 1000 V with a low-intensity laser light source. The fit function (see details in Ref. [21]) is shown as a solid line. The relevant parameters (see text) are $\mu = 0.0052$, $\gamma_{\text{average}} = 15.53$, and scale = 327 fC. This corresponds to a MaPMT gain of 2.0×10^6 .

The characteristics of the SPE spectrum were studied using the charge measurement functionality of the slow shaper of the MAROC3 chip. A new computational model [21] for the description of the PMT response functions of both the H8500 and H12700 MaPMTs was developed. Important features of the model include the ability to approximate the true SPE spectra from different PMTs with a variety of parameterized spectral shapes. The predictive power of the model was tested by demonstrating that the SPE spectral parameters, obtained in the measurements, well describe the amplitude distributions of the same photodetector measured at different levels of illumination. Thus, the model allowed us to extract the characteristic parameters of the devices independently of the test measurement conditions.

The SPE spectrum is extracted by fitting the signal amplitude distribution with the model function measured as shown in Fig. 13 for the H8500 MaPMT and in Fig. 14 for the H12700. The x-axis is calibrated in terms of charge measured by the MAROC3 chip. To approximate the performance of the first amplification cascade of the MaPMTs, the probability function was introduced in the model as a trinomial sum of three Poissonian distributions with different average secondary

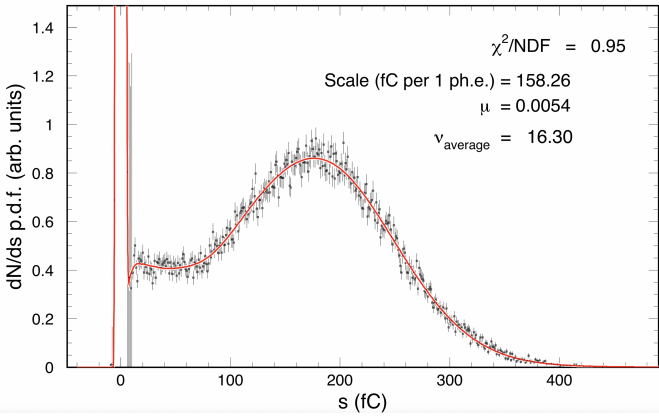


Figure 14: Sampled H12700 MaPMT single photoelectron spectrum from one of the pixels at 1000 V with a low-intensity laser light source. The fit function (see details in Ref. [21]) is shown as a solid line. The relevant parameters (see text) are $\mu = 0.0054$, $v_{average} = 16.3$, and *scale* = 158.26 fC. This corresponds to a MaPMT gain of 0.98×10^6 .

395 multiplicities and the corresponding three relative probabilities
 396 for every photoelectron to generate secondary electrons (see
 397 Ref. [21] for more details). In each fit, the parameter μ
 398 corresponds to the average number of photoelectrons generated
 399 at the photocathode by each laser pulse, $v_{average}$ is the average
 400 number of secondary electrons generated at the first dynode,
 401 and *scale* is the average anode charge collected from one
 402 photoelectron.

403 In the single-photoelectron amplitude spectra shown in
 404 Figs. 13 and 14, the normally significant contributions of the
 405 cross-talk signals, caused by the photoelectron amplification
 406 cascades in the neighboring PMT channels, have been removed
 407 by using the filter masks covering the neighbors, and leaving
 408 open only the pixel studied. The detailed discussion of the
 409 method will be given in [22]. The data showed that the H12700
 410 has, on average, a 10% better efficiency than the H8500, likely
 411 due to the improved photocathode performance and collection
 412 efficiency. An example of the results for one MaPMT is shown
 413 in Fig. 15. The parameter *scale* (top plot), characterizing
 414 the amplification (dynode) system, is virtually independent of
 415 the light radiation level, while strongly dependent on the high
 416 voltage setting, the exact behavior one would expect from the
 417 characteristics of the internal dynode system of a MaPMT.
 418 The central plot shows the average number of photoelectrons
 419 μ measured with different optical filters. It indicates that all
 420 of the channels respond in the same way as the light intensity
 421 increases. This parameter is practically independent of the
 422 applied voltage, as expected. The parameter $v_{average}$ (bottom plot)
 423 that is related to the first dynode performance, has a weak
 424 dependence on the bias voltage and is independent of the level
 425 of light radiation as well.

426 The results of the characterization have been stored in the
 427 CLAS calibration database and are available for use in the
 428 Monte Carlo simulations. The extracted gain values have been
 429 used to perform the equalization of all 25024 readout channels.

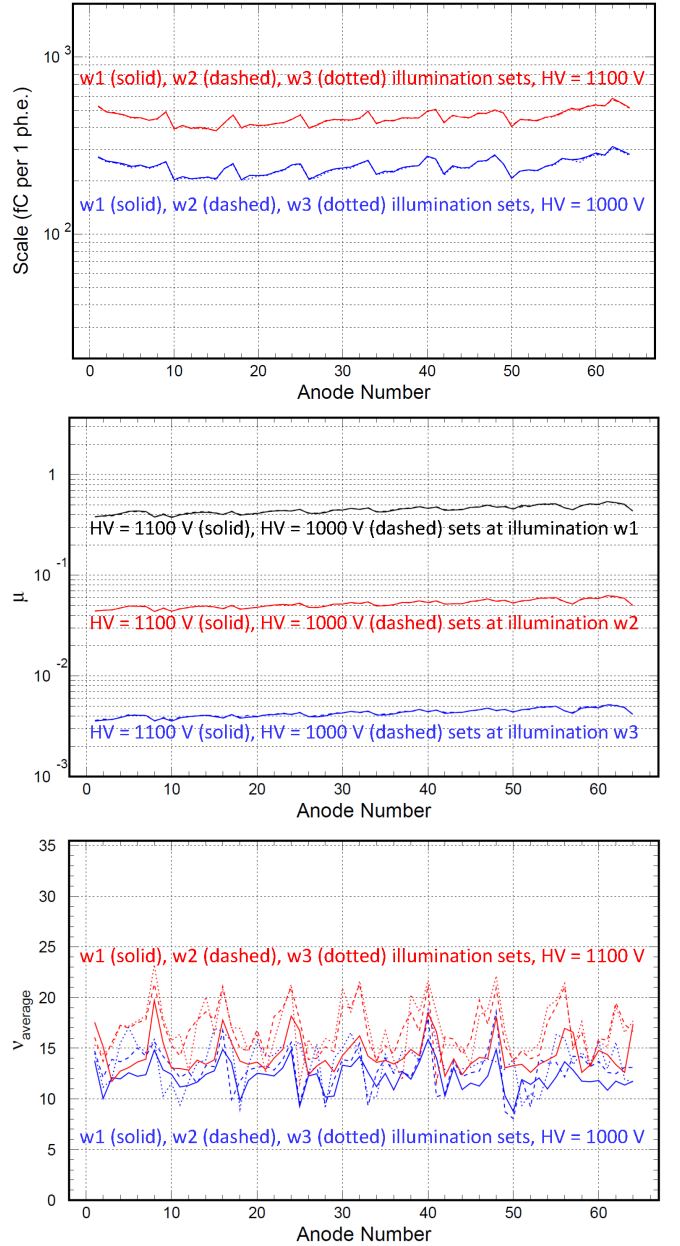


Figure 15: Distributions of fit parameters measured at 2 different high voltages (1000 V and 1100 V) and 3 different light intensities ($w_1:w_2:w_3 \sim 100:10:1$) for 64 pixels of one MaPMT: the parameter *scale* characterizing the dynode amplification system (top), the average number of photoelectrons μ (center), and the first dynode amplification v (bottom).

430 The SPE spectra allow for the study of the SPE response
 431 dependence on the working parameters, i.e. MaPMT bias
 432 voltage, MAROC pre-amplification gain, and discriminator
 433 threshold ² using the binary readout line. Data indicated that
 434 the efficiency reaches a plateau over a wide range of working
 435 parameter values [18]. The plateau corresponds to the region
 436 where all of the MaPMT discharges are digitized and the
 437 efficiency ultimately depends on the quality of the
 438 photocathode. The plateau is a consequence of the saturated
 439 mode employed in the MAROC binary readout and allows a
 440 flexible definition of the working point, a crucial feature when
 441 dealing with a large number of channels in the challenging
 442 single-photon regime.

443 3.4. The Detector Services

444 The CLAS12 RICH requires various services, namely power,
 445 cooling, and gas purge whose number of lines has to be
 446 minimized and installed outside of the CLAS12 acceptance.
 447 A continuous nitrogen flow, supplied by the Hall B gas
 448 distribution system, is provided in order to keep the relative
 449 humidity inside the RICH vessel at a few percent level. The
 450 flow is set to about 40 liters per minute to ensure a complete
 451 inner volume exchange every few hours. A backup system has
 452 been realized by a stack of nitrogen bottles to allow for up to
 453 3 days of gas flow in case of failure of the primary distribution
 454 system.

455 The electronics power is controlled by a CAEN SY4527
 456 power supply with five 8-channel A2518 low voltage (LV)
 457 boards and five 32-channel A1536 high voltage (HV) boards.
 458 Each LV channel powers 4 readout units, while each HV
 459 channel drives the MaPMTs grouped in one readout unit. The
 460 electronics readout is connected to the back-end by three MTP
 461 trunks of 2.5 Gbps optical fibers. One trunk groups several
 462 multi-core fibers, each of them connecting one of the eight ports
 463 in the VME/SSP [20] back-end module to four FPGA boards.

464 The readout electronics dissipates about 3.5 W per unit,
 465 mainly due to the FPGA chip and the optical transceiver, as
 466 shown by the thermo-camera image in Fig. 16. The total
 467 heat load, at the level of 500 W, is removed by a forced air
 468 flow. Since the electronics panel is not fully sealed due to the
 469 numerous holes for the readout and HV connectors, there is a
 470 diffusive exchange in the RICH vessel between the nitrogen gas
 471 used to keep the aerogel dry and the air in the electronics panel.
 472 As a consequence, dry and clean air is required to cool down the
 473 electronics. This is achieved with an Altas Copco multi-core
 474 oil-free rotary scroll air compressor. The compressor fills a
 475 tank at 8 atm pressure, from where the cooling air is filtered
 476 and circulated toward two distributors located at the sides of the
 477 electronics panel and outside the acceptance. These are made
 478 of stainless-steel tubes with several nozzles to direct the cooling
 479 air supersonic flow along the board surface. The exhaust is
 480 made of six corrugated tubes that run in the back of the RICH
 481 module behind the spherical mirror.

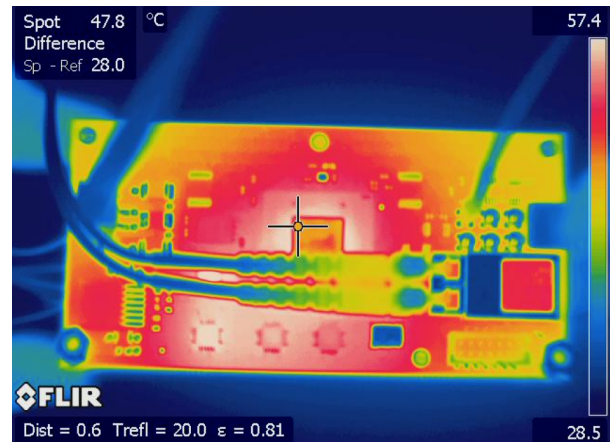


Figure 16: The CLAS12 RICH readout unit as imaged by a thermo-camera. The hottest spots are the FPGA chip in the center and the optical transceiver on the right.

4. The RICH Detector Installation and Commissioning

4.1. RICH Assembly

The assembly of the RICH detector was performed in a clean room and each element was installed after the completion of the relative characterization tests. The trapezoidal RICH vessel was attached to a large aluminum structure with a pivot to rotate the detector from the vertical to the horizontal position, as required by the various assembly phases.

The ten spherical sub-mirrors were mounted on a common frame inside the RICH vessel. To minimize the material budget, the frame is composed by a net of 1.5-mm-thick carbon-fiber U-profiles. Each element (frame and sub-mirrors) has three mounting points designed to allow precise alignment. The relative alignment of the sub-mirrors was performed with the same setup used to determine their surface accuracy. The full spherical mirror was illuminated by a point-like source and the position of each sub-mirror was adjusted until the ten spot images converged into the nominal center of curvature. In Fig. 17, the reflected images before the alignment (when each sub-mirror produces a spot at a different location) and after the alignment (when all the spots overlap within a few mm) are shown. The quality of the result is also visible in Fig. 18, where the spherical mirror system before (left) and after (right) the alignment is shown.

The lateral and bottom planar mirrors were attached to the RICH trapezoidal vessel structure by means of joints that allow for a precise alignment. The two front mirrors were mounted on the lower front panel made of carbon fiber. The relative position of the mirrors was aligned with respect to the RICH vessel at the level of about 0.5 mrad by using a faro-arm. The fully installed mirror system as seen from the entrance panel is shown in Fig. 19.

The RICH photon detectors and readout electronics were installed on the electronics panel using an independent aluminum support structure to enable easy access and to allow rotations during the functionality tests. The PMTs with higher gain

²The programmed threshold levels are expressed in Digital-to-Analog Converter (DAC) units, 1 DAC unit corresponds to about 1 mV.

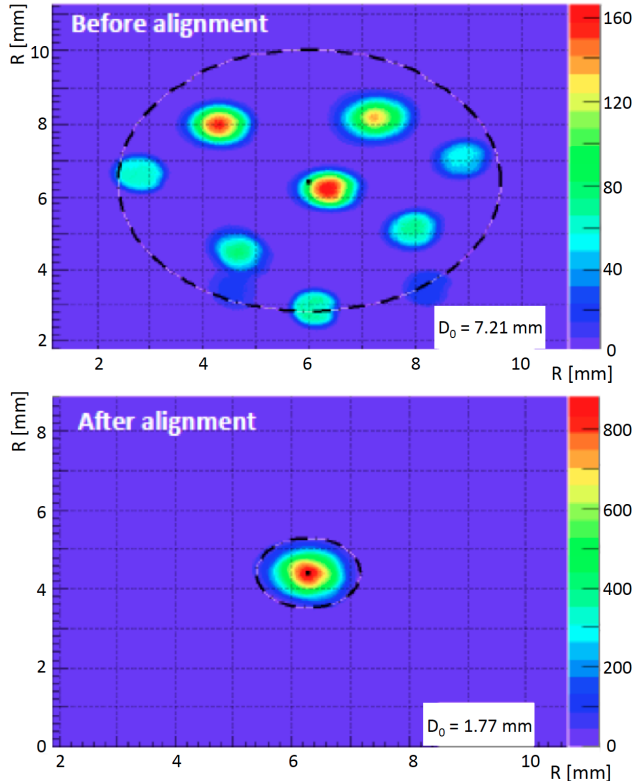


Figure 17: Reflected spot by the whole spherical mirror system: before the alignment (top plot), all sub-mirrors image the light source in different locations; after the alignment (bottom plot), all images overlap in the same position. The spot brightness depends on how close the sub-mirror center is to the sensor position.



Figure 18: The spherical mirror before (top plot) and after (bottom plot) alignment. As a result of the alignment, the image appears continuous along the whole mirror surface.

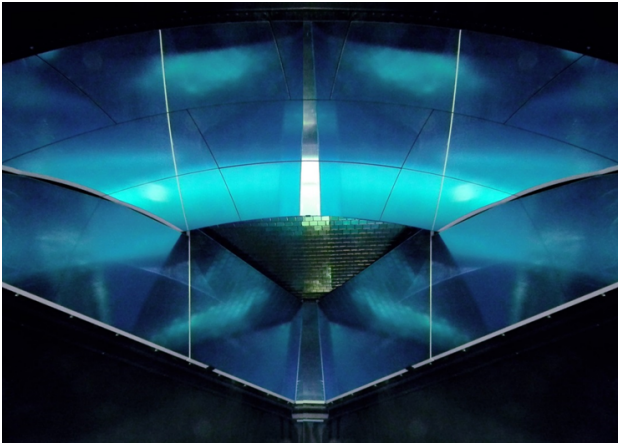


Figure 19: The mirror system as it is seen from the RICH entrance panel. Clockwise from the top, the ten spherical sub-mirrors, the two right lateral mirrors, the bottom mirror, and the two left lateral mirrors are visible. At the center, the MaPMT array is also visible.



Figure 20: The fully assembled plane of MaPMTs.

were placed closer to the beam pipe, where better detection performance is required. As the MaPMT in one readout unit share the same HV bias, they were selected to be of similar gain and of the same type (H8500 or H12700). The fully equipped electronics panel is shown in Fig. 20 from the MaPMT side and in Fig. 21 from the readout electronics side.

After the electronics panel assembly was completed, particular care was devoted to minimize and stabilize the pedestal width values. The measured pedestal RMS was initially at the level of few DAC units, with relatively large variations not only from MaPMT to MaPMT but also among the channels of a single MaPMT, as shown in the top plot of Fig. 22. As the readout uses a single threshold value per chip (or MaPMT), the channel-by-channel variation may effect the single channel efficiency in a way that would be complicated to correct for. Therefore, a grounding grid was realized by connecting all of the components of the readout system, powered by the floating 5 V low-voltage lines, were properly referred to



Figure 21: The fully assembled and cabled front-end electronics. Visible are the gray 20 AWG LV cables, the red HTC-50-1-1 HV cables, and the cyan MTP optical fibers.

the same ground. This reduced the typical pedestal RMS down to about 1 DAC unit, a level comparable with the test bench results, as shown in the bottom plot of Fig. 22.

Several tests were performed using cosmic rays at various stages of the electronics assembly. In the absence of a precise measure of the cosmic particle momentum, it was not possible to perform any study of the Cherenkov angle resolution. Nevertheless, cosmic runs allowed for the validation of the translation tables relating the electronics channels to the pixel positions, the development of the ring reconstruction software, the verification of the stability of the system, and the testing of the performance of the power supplies, cooling, readout, slow controls, and interlock services. After all planned tests were completed, the complete readout system was eventually transferred into the mechanical structure.

The aerogel was the last element installed, being the most sensitive to the external conditions. For this reason, before its assembly, a test to verify the gas-tightness of the RICH vessel, temporarily completed with all of the closing panels, was performed. Each aerogel tile was inspected and mounted in a pre-selected location of the supporting structure, namely the front mirrors for the 2-cm tiles and the upper front panel for the 3-cm tiles. The location of each tile was determined in order to concentrate the tiles with the higher expected photon yield at forward polar angles where the particle identification requirements are most demanding. In addition, tiles with close optical properties were coupled in the same location of the double 3-cm layer. The tiles were secured in place by a net of nylon wires that ran along the edges and, on the side, by plastic bumpers covered by a thin foam layer to avoid damage to the aerogel. The tiles were also optically isolated from each other by using a thin layer of foam stretched around each tile. In fact, photons produced in one tile and propagating through an adjacent tile undergo surface effects that generally degrade the angular resolution. The foam is instrumental to avoid sharp edge contacts between the blocks that might originate cracks in the aerogel material. In addition, the foam net bonds the tiles together in forming a sole and stable layer. Figure 23 shows the front planar mirror system with the aerogel tiles fully installed.

During the assembly, the aerogel panels were maintained in

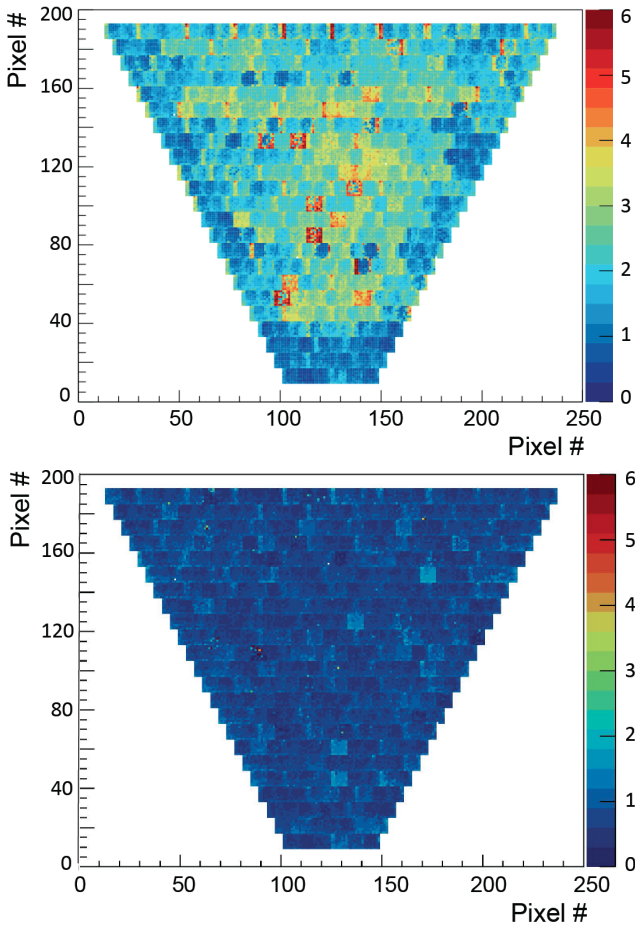


Figure 22: Map of the pedestal RMS values before (top) and after (bottom) the realization of a grounding grid connecting all of the electronics units to the RICH chassis to provide a common ground reference for the floating power lines.

577 a low-humidity atmosphere (around 20% relative humidity) to
 578 prevent moisture absorption. Once the assembly of all tiles
 579 was completed, the panels were quickly installed on the RICH
 580 vessel, the detector was sealed with all of the closing panels and
 581 a flow of purged nitrogen was started to minimize the exposure
 582 to the external environment conditions.

583 Once the detector was sealed and before the transportation to
 584 the experimental hall, its functional parameters were tested for
 585 several weeks in the assembly room. The tests included the two
 586 gas systems serving the RICH: the nitrogen system that must
 587 keep the internal humidity at the few percent level to preserve
 588 the aerogel optical performance and the air-cooling system of
 589 the readout electronics.

590 4.2. RICH Commissioning

591 The RICH detector was installed in the CLAS12 spectrometer
 592 at the beginning of January 2018, in time with the start
 593 of the first data taking in Hall B. In preparation for the data
 594 taking, a number of tests were routinely performed without and
 595 with beam to establish the running conditions and to verify the
 596 stability of the response.

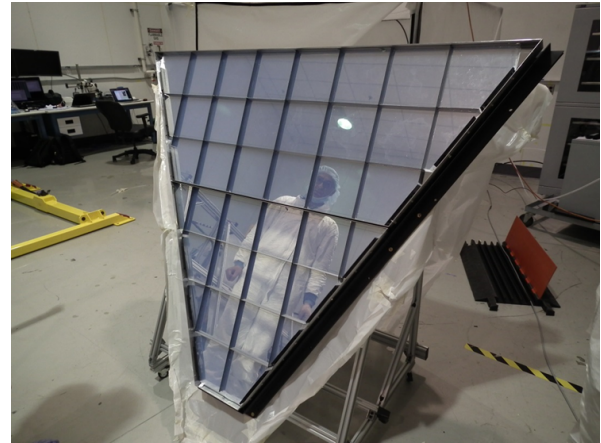


Figure 23: The 2-cm-thick section of the aerogel mounted on the two RICH front mirrors. Visible are the external aluminum frame and the black foam net that optically and mechanically isolates each tile from the others.

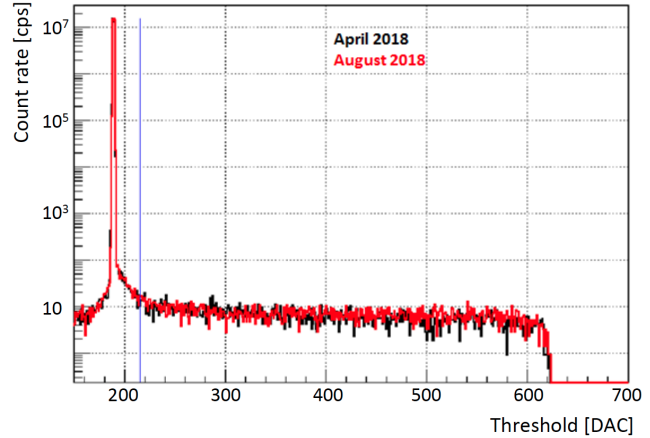


Figure 24: Example of a SPE spectrum from the dark rate measurement of one readout channel as a function of the threshold value. The two histograms were recorded in April and August 2018. The blue line indicates the threshold setting.

The basic tool to monitor the RICH front-end electronics is provided by the measurement of the MaPMT dark noise counting rate. The number of counts above a programmed threshold is recorded for a time period on the order of a second. A fine scan of the threshold value allows for the reconstruction of the full SPE spectrum for each of the 25k channels. An example of one SPE spectrum is shown in Fig. 24. The main features of the data are: *a*) a very narrow pedestal where the threshold equals the analog baseline, *b*) a region close to the pedestal where the rate smoothly decreases as the threshold increases (corresponding to the almost linear regime of the MAROC), and *c*) a large plateau of the saturation regime, where the count rate is basically insensitive to the threshold setting almost up to the edge of the SPE region. The plateau is a crucial feature of the front-end electronics, because it allows a flexible definition of the working point without the need for extreme precision in the channel equalization. Counts at threshold

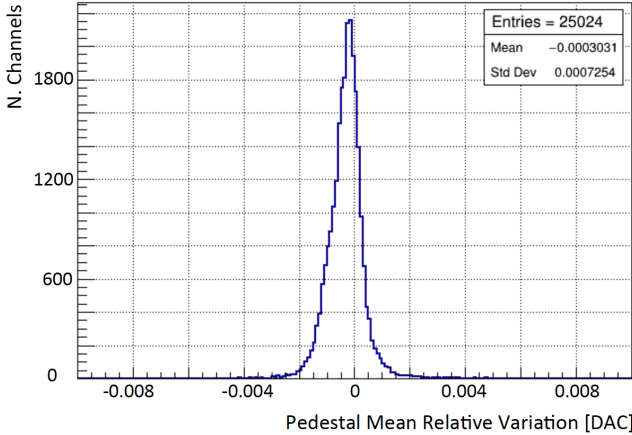


Figure 25: Relative variation of the mean pedestal position of the 25024 readout channels between April and August 2018.

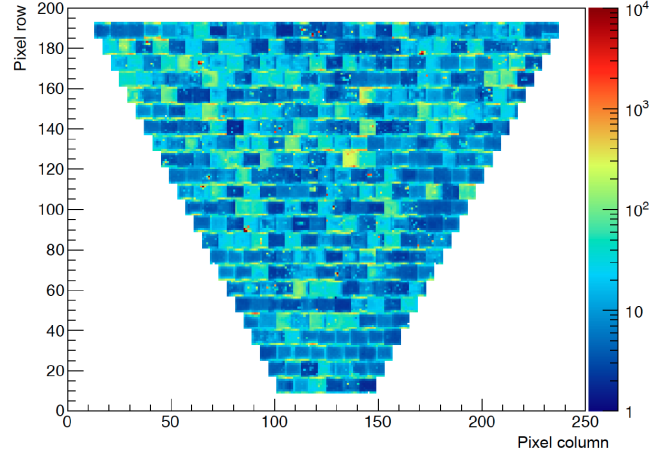


Figure 27: Map of the average dark count rate in the plateau region of threshold values (color scale).

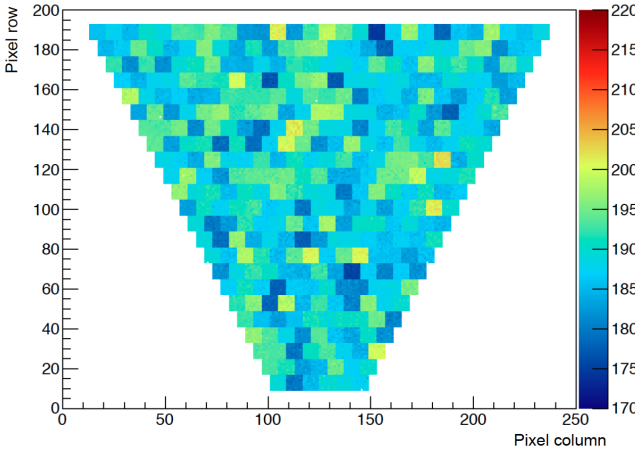


Figure 26: Map of the mean pedestal position in DAC units (color scale).

values below the pedestal are due to the bipolar shaped signal.
The spectra allow for the channel-by-channel extraction of the
pedestal position and width, the dark count rate in the plateau
region, and the amplitude of the SPE region. The black and
red histograms in Fig. 24, taken in April and August 2018,
respectively, demonstrate the stability of the readout system
over several months of running. Moreover, in Fig. 25, the
relative variation of the mean pedestal position in the same
interval of time is shown. On average, the pedestals are stable
at the level of 10^{-3} .

The pedestal level is different for each readout channel, but it is quite uniform within one MAROC chip, as can be seen from the map shown in Fig. 26. This result guarantees the effectiveness of the common threshold.

The average count rate in the plateau region provides a measurement of the dark count rate of the channel, as shown in the map of Fig. 27. The typical dark count rate is a few tens of Hz, with more than 99% of the channels below 100 Hz and only few channels above 10 kHz. It is also found that the highest dark count rates in the MaPMTs are located in the first

and last row of pixels. Although measured with a completely different setup, these results are in good agreement with the values quoted in the Hamamatsu data sheets.

The MAROC preamplifier equalization gains are determined using the characterization measurements described in Section 3.3.3 by tuning the average MaPMT+MAROC gain to 2.7×10^6 in all channels. The equalization gains range from about 0.5 to 3, with an average value of 1.2. The effect of the channel-by-channel signal equalization was verified during the engineering run by taking data at various thresholds for different MAROC gain configurations. Figure 28 shows the ToT distribution for three typical values of the threshold, on the top for all channels without amplification (nominal MAROC gain of 1) and on the bottom after equalization. After equalization, the ToT distribution of saturated SPE signals is narrower than with unitary gains. With typical ToT values larger than 40 ns, the signal region is also clearly separated from the cross-talk signals whose ToT values are distributed around 25 ns.

After these tests, the common discriminator thresholds were set to +25 DAC units above the average MaPMT pedestal position, a level that corresponds to a small fraction of the average SPE amplitude.

4.3. RICH Slow Controls and Interlocks

The RICH slow controls are based on Experimental Physics Industrial Control System (EPICS) [23]. It includes EPICS input-output controllers (IOCs) interfacing with different types of hardware via communication protocols and over 25k RICH process variables (PVs). The controls system monitors many aspects of the RICH detector, such as the scaler rates of all 25k Hamamatsu MaPMT pixels, the FPGA temperatures of each readout board, the HV and LV power supplies, the LV and current consumption of each readout unit, the gas system, and the temperature and humidity of the electronics panel volume and detector volume. For the Graphical User Interface (GUI), the Control Systems Studio (CS-Studio), an Eclipse-based suite

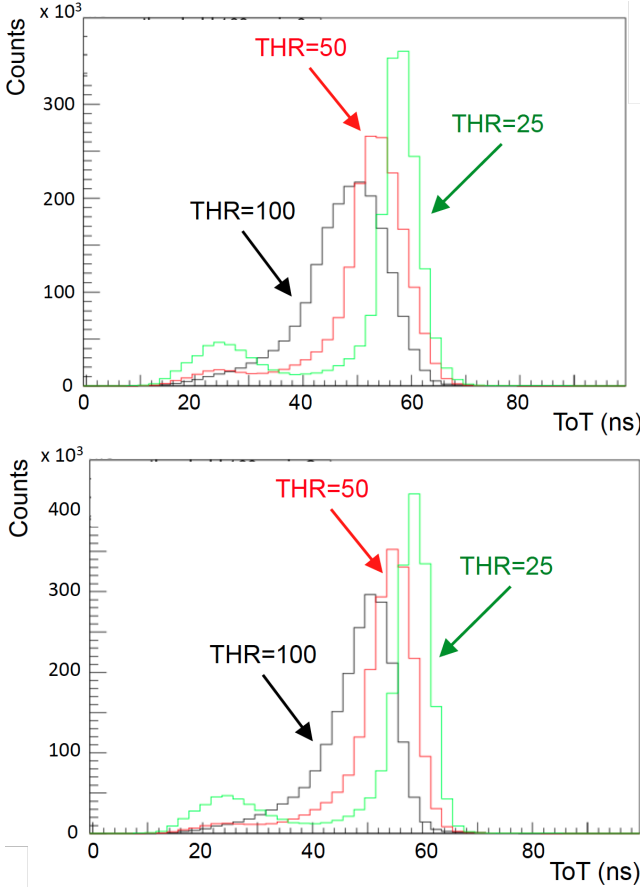


Figure 28: Time-over-Threshold (ToT) distributions of the RICH channels at three typical values of threshold (25, 50, and 100 DAC) without (top) and with (bottom) gain equalization. The saturated SPE signals generally yield ToT durations greater than 40 ns. When lowering the threshold weaker cross-talk signals are also recorded with ToT durations around 25 ns. Figure taken from Ref. [18].

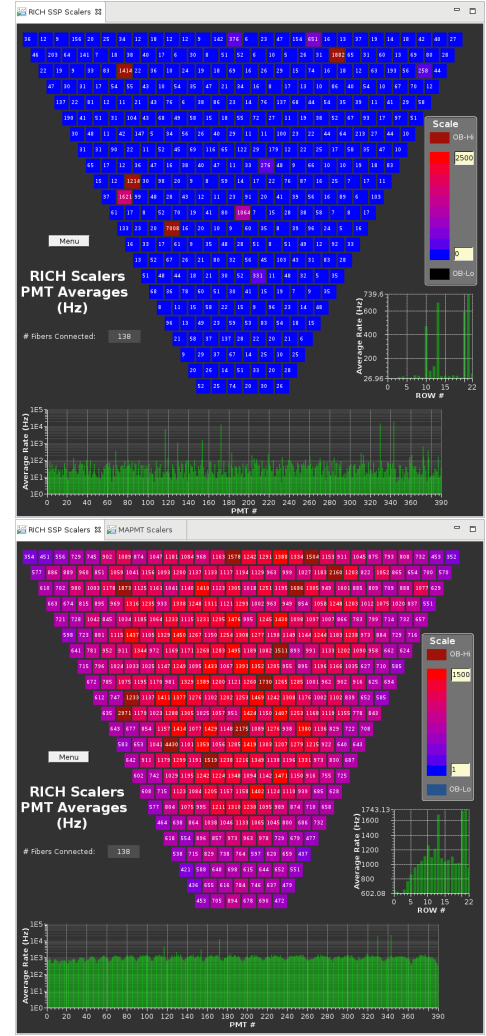


Figure 29: The average count rates (in Hz) over 64 pixels for each MaPMT during data taking. Top: without beam on target, Bottom: with beam on target. High count rates in absence of beam are typically due to a single hot channel in the MaPMT.

of tools for developing and monitoring large-scale control systems, is used.

The quality of the data is monitored by scaler and TDC plots. Figure 29 shows the average MaPMT rate measured by the scaler readout system when the beam is off (top plot) and when the beam is on (bottom plot). In the top plot, the few MaPMTs where the dark rate is substantially higher than the average can easily be seen. This is typically due to a single hot pixel in the MaPMT. The bottom plot shows that when the beam is on the rate is always dominated by physics events. Figure 30 shows the occupancy plots from the TDC readout. The top plot shows the occupancy per channel, and the center and bottom plots show the distributions of the leading and trailing edge times per MaPMT, respectively. All of these plots are used during the data taking to identify possible malfunctioning channels and, eventually, restore them through a recovery procedure.

The slow controls and monitoring of the RICH detector is enforced by the hardware interlock system based on the National Instruments CompactRIO (cRIO) [24]. The cRIO system monitors the following parameters:

- Temperature and humidity in 16 locations of the detector volume;
- Temperature and humidity in 16 locations of the electronics panel;
- Air tank pressure;
- Air and nitrogen flow.

The locations of the temperature and humidity sensors, and the air and nitrogen flows fed into the electronics panel and nitrogen volume are shown in Figs. 31 and 32, respectively. The inner temperature of the electronics panel ranges between 38.5°C and 44.5°C moving from the bottom towards the top of the module, whereas the external temperature stays below 34.5°C, in accordance with the requirement to not drive the FTOF system above 40°C. The relative humidity is below 0.5%. In the nitrogen volume, the temperature ranges between 23°C

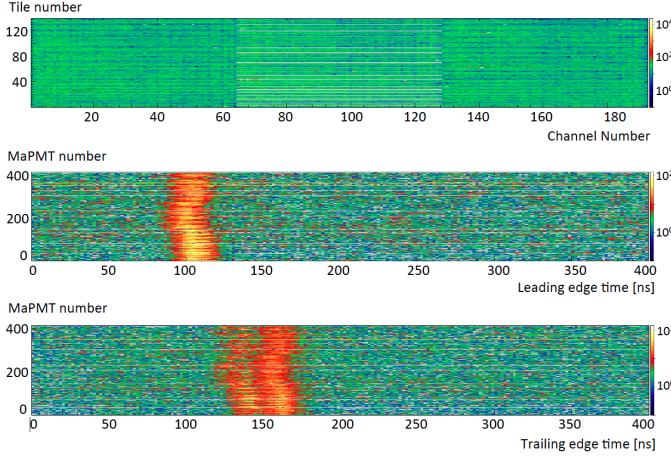


Figure 30: Online monitor plots of the TDC occupancy with beam on. From top to bottom: channel occupancy in terms of the tile vs. channel number; leading edge time distributions per MaPMT; trailing edge time distribution per MaPMT.

and 27°C. The relative humidity is below 1.3% except in the central point close to the spherical mirror pivot, where it reaches a 3% value.

The signal levels are controlled by setting limits. If the temperatures, air flow, or air pressure go out of limits, the HV and LV are powered off, i.e. interlocked. In case the humidity or the nitrogen flow are out of limits, an alarm signal is generated.

Important safety parameters of the RICH detector are: the temperature of the front-end electronics, the gas flow, and the RICH internal relative humidity. Figure 33 presents the map of the temperatures of the front-end electronics. Typical temperature values are around 65°C on the FPGA chips and 40°C inside the electronics panel volume. The safety temperature limits are 85°C for the FPGAs, 80°C for the optical fiber cables, and 40°C for the temperature on the FTOF detector, which is about 10 cm away from the RICH. Therefore, the maximum allowed temperature was set to 75°C on the FPGA and to 45°C inside the electronics panel volume.

The nitrogen flow and the RICH internal relative humidity are measured by several probes installed inside the detector. An alarm is sent out in case the humidity exceeds 5% or in case the nitrogen flow drops below the normal value. In the latter case, the backup system starts working to restore the normal flow level and to ensure safe humidity conditions. During RICH operation, the humidity level has proven to be very stable with time.

5. The Initial Performance of the RICH Detector

5.1. RICH Event Reconstruction

The RICH reconstruction is organized in four steps. In the first step, the spatial and time information of each hit in the MaPMTs is corrected by the spatial misalignment and time calibration parameters. The hits are ordered as a function of their ToT value, as this reflects the corresponding amplitude (released charge). A 3×3 MaPMT pixel matrix centered around

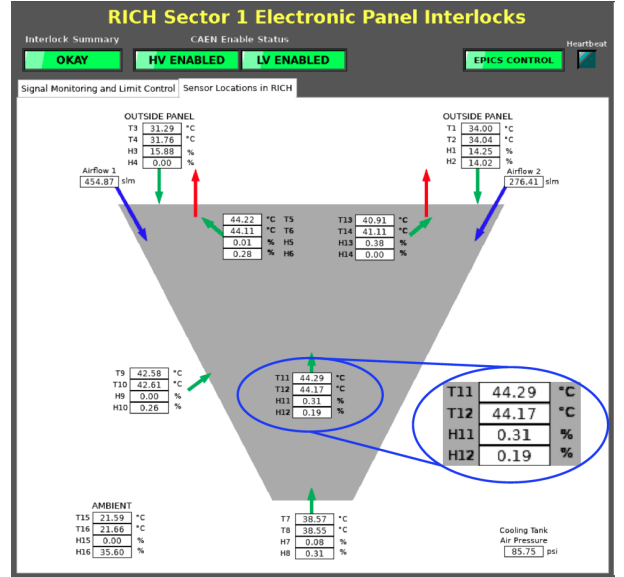


Figure 31: Location and measured values of the temperature and humidity sensors inside the electronics panel, and the cooling air input flow as measured by the flow meters of the gas line.

a local maximum, i.e. the hit with the highest local ToT, is called a nonet. If more than 3 hits are found in the same nonet they are grouped into a RICH cluster. A cluster is typically generated by a charged particle producing Cherenkov light in the MaPMT window or ionization in the sensor dynode structure. If a sole hit is found close to a local maximum with a ToT lower than 80% of that maximum, the hit is flagged as possible cross-talk. Hits belonging to the same nonet of the local maximum are flagged as optical cross-talk, while hits readout by an electronics channel adjacent to the maximum hit in the MAROC chip are flagged as electrical cross-talk. Note that the readout circuit routing has been designed to connect anodes close in space to non-adjacent MAROC3 inputs. The above selection rejects about 87% of the cross-talk hits, as can be seen in Fig. 34. In the figure, the ToT distribution of the recorded RICH hits (black solid line) is shown together with the distributions of the hits identified as optical (magenta dash-dotted line) or electrical (green dashed line) cross-talk. The shoulders on the right of the cross-talk peaks are likely due to signal discharges wrongly identified as cross-talk. The hits selected for further analysis are highlighted by the dotted (blue) histogram. The excess at low ToT values indicates a residual contamination of unidentified cross-talk. The leftover cross-talk contamination, at the level of 2.7% of the signal, can be further reduced only with a time versus amplitude analysis, see Section 5.2. The cross-talk selection also removes a small (0.8% fraction) of true Cherenkov signals. Those correspond to MaPMT discharges that undergo incomplete dynode multiplication, while being by chance close in space to another Cherenkov signal. Hits flagged as cross-talk are not considered further in the RICH reconstruction.

The second step consists in finding the spatial match between the RICH clusters and the CLAS12 charged particle tracks.

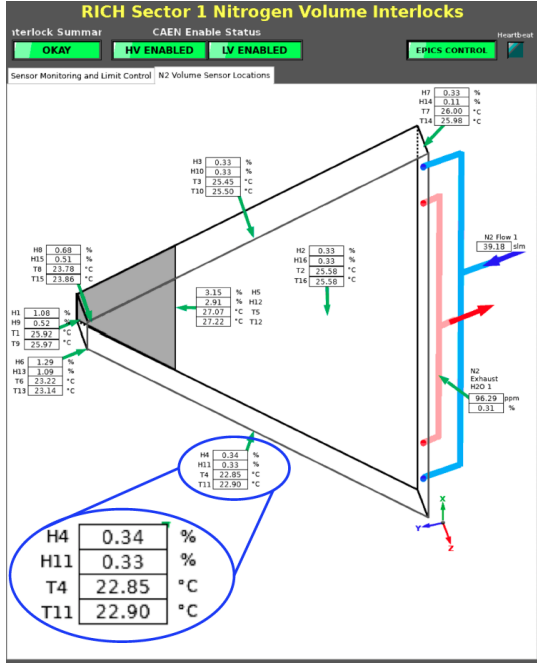


Figure 32: Location and measured values of the temperature and humidity sensors inside the nitrogen volume, and the nitrogen input flow as measured by the flow meters of the gas line.

This requires that the extrapolated impact point of the track on the MaPMT plane is within 10 cm of the cluster center. The latter is calculated as a weighted average - with the ToT value as the weight - of the spatial coordinates of all the hits in the cluster. Matched clusters allow a precise study of the MaPMT detector position and orientation relative to the CLAS12 tracking system. This is shown in Fig. 35, where the distance between the RICH clusters and the matched drift chamber tracks [25] divided by the pixel spatial RMS, a sort of χ^2 distribution, is reported. The black distribution is before and the red one is after the alignment procedure.

The third step is the core of the RICH reconstruction [26]. For each hit in the MaPMT plane, an estimate of the corresponding Cherenkov angle is derived by ray-tracing the photon path inside the RICH volume taking into account possible reflections. This is done in turn for each charged particle traced through the RICH, with the photon emission point assumed to be the middle point of the particle path inside the aerogel radiator. In the fourth step, a particle identification algorithm is applied using an event-based likelihood of the reconstructed Cherenkov angles and times.

5.2. RICH Time Resolution

The time information of the RICH hits is provided by the leading edge time T_1 measured by the TDC implemented into the FPGA board with a 1-ns precision. In-time photon hits are selected by comparing their T_1 with the time T_{calc} computed using the CLAS12 information (see Fig. 36). T_{calc} comprises the event start time, the charged track path and flight time provided by the tracking system, and the Cherenkov photon

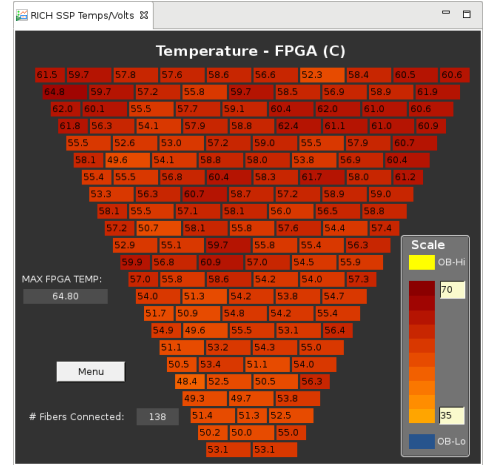


Figure 33: Slow controls display: Map of the temperatures measured on the FPGA chips.

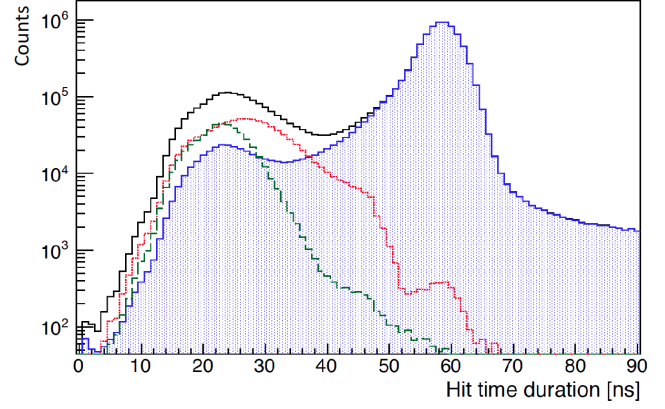


Figure 34: ToT distribution of the recorded RICH hits (black solid line) together with the optical (magenta dash-dotted line) and electrical (green dashed line) cross-talk distributions. The hits selected for further analysis are highlighted by the blue dotted histogram.

path reconstructed inside the RICH as explained in Ref. [26]. Being based on the precise FTOF system [3] and the accelerator RF frequency, the CLAS12 computed time features a time resolution on the order of 100 ps, significantly better than RICH. The CLAS12 computed time can therefore be used as a reference for the RICH time calibration.

With respect to the expected time resolution, significant channel-by-channel variations are found in the difference between the measured and the calculated times as shown in the top plot of Fig. 37, where the distribution of $\Delta T = T_1 - T_{calc}$ as a function of the channel number is shown. These variations are introduced by the readout chain, with the biggest contribution coming from the average length of the 3 optical DAQ fiber trunks and from the specific length of the various fibers in each trunk. Smaller variations among the individual channels of one board can also occur due to the different circuit routing and components. An additional overall time constant is expected from the relative calibration of the RICH with respect to the

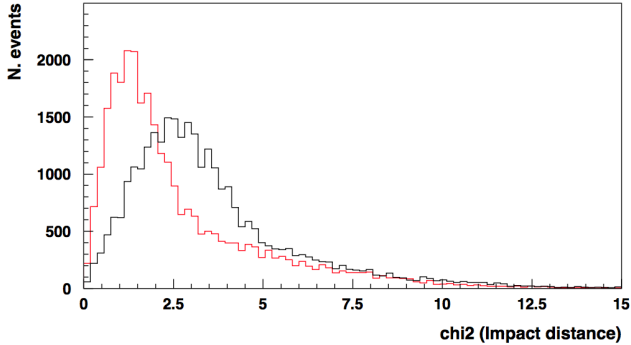


Figure 35: RICH matching χ^2 , defined as the distance between the RICH clusters and the matched drift chamber tracks divided by the pixel spatial RMS. The black distribution is before and the red one is after the alignment procedure.

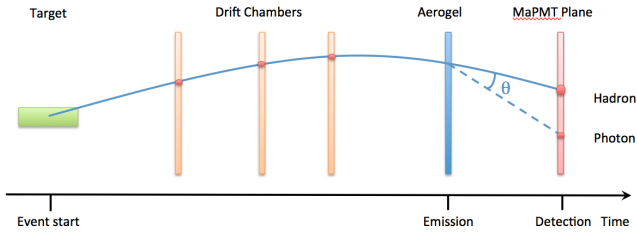


Figure 36: The RICH photon detection time as measured by the CLAS12 spectrometer. It is defined as the event start time plus the flight-times of the hadron from the interaction point to the radiator center and of the ray-traced photon within the RICH volume.

rest of the CLAS12 detectors.

A broadening of the ΔT distributions is due to the time walk, i.e. the dependence of the trailing edge time on the amplitude of the input signal. Since the MAROC3 readout mostly works in the saturated regime already at the SPE level, this effect is expected to be relevant for small amplitude signals, as can be seen from the bottom plot of Fig. 37. Saturated signals have typical ToT values on the order of 60 ns, while small amplitude signals are expected to be discriminated up to several ns later. The vertical band at $\text{ToT} \approx 60$ ns comprises a distribution of random-time MaPMT dark counts and off-time beam bunches. The independent excess around $\text{ToT} \approx 25$ ns signals a residual contamination of cross-talk pulses as anticipated in Section 5.1.

A two-step calibration procedure was implemented in order to align the time measured from all RICH readout channels with the expected (calculated) one. The current version of the software uses electrons and charged pions identified in CLAS12 with momenta larger than 2.5 GeV/c and Cherenkov photons reconstructed in the RICH with no reflections on the mirrors.

The first step of the procedure consists in the evaluation of the 25024 time offset corrections. The values of ΔT are plotted for each channel and the position of the maximum is taken as the time offset for that channel. The top plot of Fig. 38 shows a typical ΔT distribution, with a pronounced peak, a broad tail due to the time walk, and a small enhancement above ≈ 10 ns most likely due to residual cross-talk hits. The vertical line indicates the adopted value for the time offset correction.

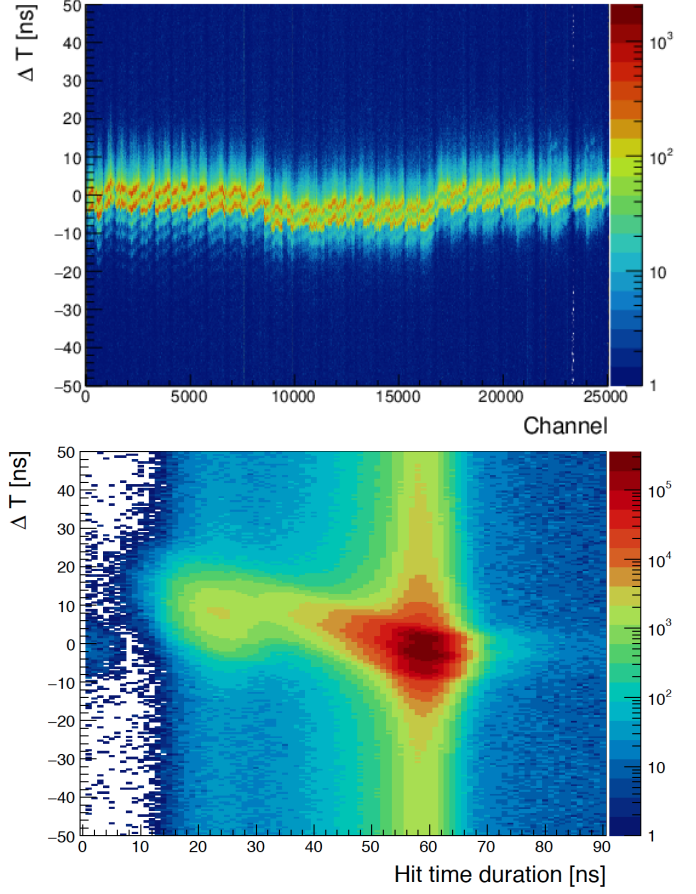


Figure 37: Top plot: distribution of the time difference ΔT between the measured RICH and calculated CLAS12 times as a function of the RICH readout channel. Bottom plot: cumulative distribution of the time difference ΔT as a function of the hit duration time (ToT).

The bottom plot of Fig. 38 shows a typical map of the time offsets. Three regions of comparable values are highlighted, corresponding to the tiles connected to the 3 optical fiber trunks, on top of smaller channel-by-channel variations.

Once the individual channels were corrected for the time offsets, the time-walk corrections were extracted from the ΔT distribution as a function of ToT. Since the threshold level is common to all channels of one MAROC3 chip, and the amplitude equalization has been performed, one expects that the same time-walk correction should work for all channels of one MaPMT. This was verified by comparing plots like the one shown in the bottom plot of Fig. 37 for all channels of the MaPMTs. A set of 391 time-walk correction functions, one per MaPMT, is therefore extracted by fitting the dependence of ΔT as a function of ToT, as shown in the top plot of Fig. 39. The dependence is fit with two lines, one for the saturated regime and one for the linear region:

$$\begin{aligned} \text{ToT} < \text{ToT}_0 & : m_1 \text{ToT} + \Delta T_0 \\ \text{ToT} > \text{ToT}_0 & : m_2 \text{ToT} + (m_1 - m_2) \text{ToT}_0 + \Delta T_0 \end{aligned} \quad (2)$$

The free parameters of the fit are the two slopes m_1 and m_2 ,

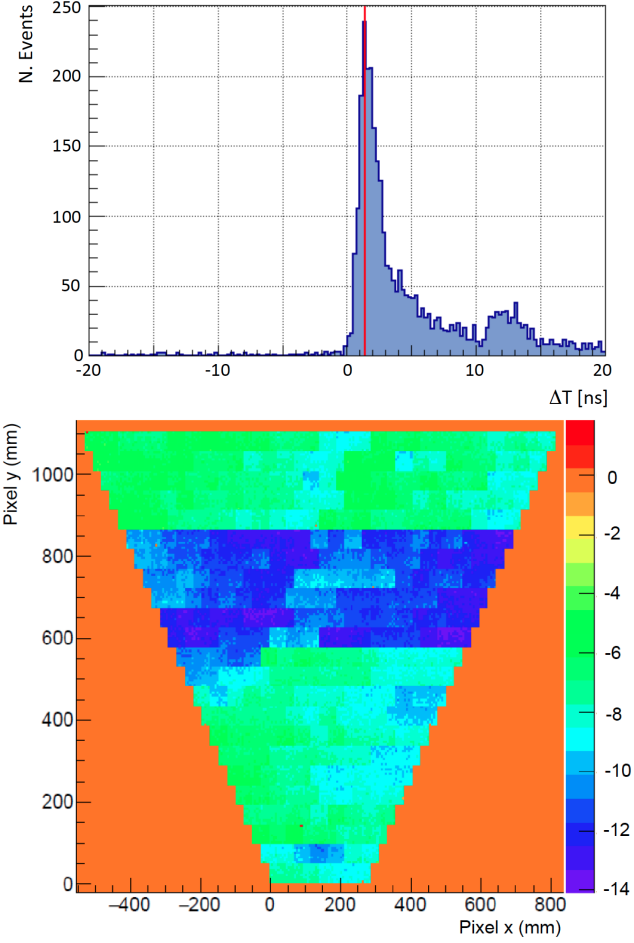


Figure 38: Top plot: ΔT distribution for one readout channel; the red line indicates the time offset value. Bottom plot: typical map of the time offsets.

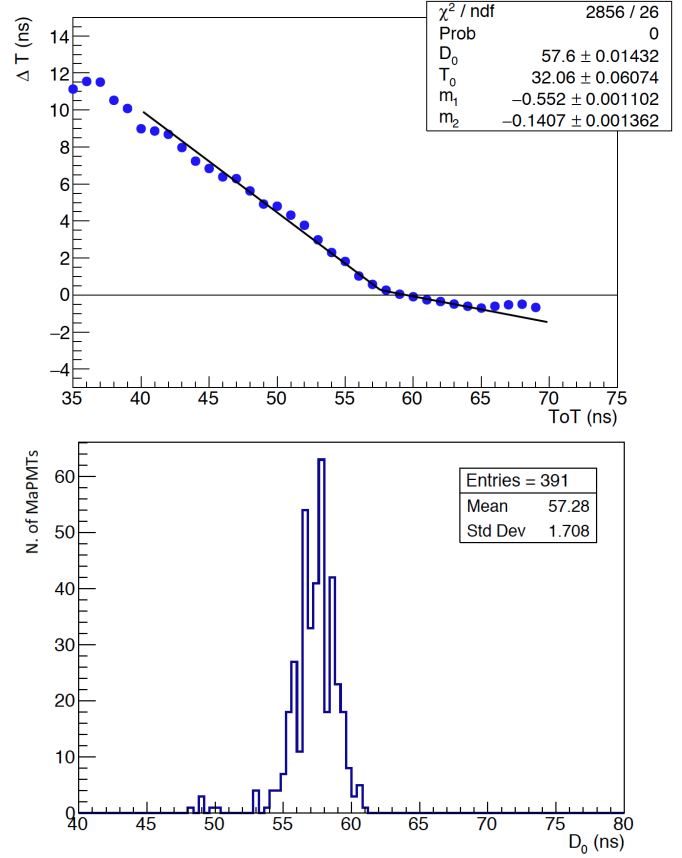


Figure 39: Top plot: fit of the time-walk correction for one MaPMT. Bottom plot: distribution of the ToT saturation values extracted from the time-walk corrections.

864 the value ToT_0 where the two lines cross, i.e. the ToT saturation
 865 value, and the value ΔT_0 at zero ToT. The data show small
 866 deviations from the linear behavior. However, such a simple
 867 functional form was adopted to minimize the probability of
 868 fit failure (having to deal with several hundreds of fits) and
 869 because it was proven to be enough to achieve time resolutions
 870 that meet the specifications. In the bottom plot of Fig. 39, a
 871 typical distribution of the saturation ToT values obtained from
 872 the fit is shown. The average value is around 57 ns with small
 873 variation from MaPMT to MaPMT.
 874

875 After calibration, the corrected ΔT distribution is centered
 876 at zero for all channels, see Fig. 40. As a consequence,
 877 few ns time coincidence can be applied to remove the spurious
 878 hits. As shown in the bottom panel of Fig. 40, the cross-talk
 879 hits at $ToT \approx 25$ ns and the 4.008 ns sub-structure of the
 880 off-time beam bunches at $ToT \approx 60$ ns become clearly visible.
 881 A typical ΔT distribution is shown in Fig. 41, where the red
 882 and black histograms show the ΔT values before and after the
 883 correction, respectively. The red curve is a Gaussian fit of
 884 the corrected distribution. On average, we obtained a time
 885 resolution $\langle \sigma \rangle \approx 0.7$ ns, well below the requirement of 1 ns.
 886

5.3. RICH Hadron Separation

The RICH has been designed to provide hadron identification in the 3 GeV/c to 8 GeV/c momentum range. The most challenging separation is between kaons and pions, as their Cherenkov angles become closer and closer with the increase of momentum until a minimum difference of 6 mrad at 8 GeV/c. In addition, in this momentum range the pion yield is more than an order of magnitude larger than for the other hadron species. The RICH Cherenkov angle reconstruction relies on the performance of the CLAS12 tracking system, able to provide tracks with momentum resolution better than 1% and polar angle resolution better than 1 mrad [4].

Various ring imaging topologies are possible due to the unconventional RICH geometry. These topologies are generated by direct photons in proximity focusing and by reflected photons in mirror focusing geometries. In the momentum range of interest (between 3 GeV/c and 8 GeV/c), electrons can be used for a detailed optimization of the RICH performance since, being in a saturated regime, their Cherenkov angles are indistinguishable from those of pions. The work is still ongoing to make use of the large recorded electron statistics.

Examples of reconstructed RICH events are shown in Figs. 42 to 45 for particles identified as electrons by CLAS12. In each figure, the reconstructed RICH event is displayed on

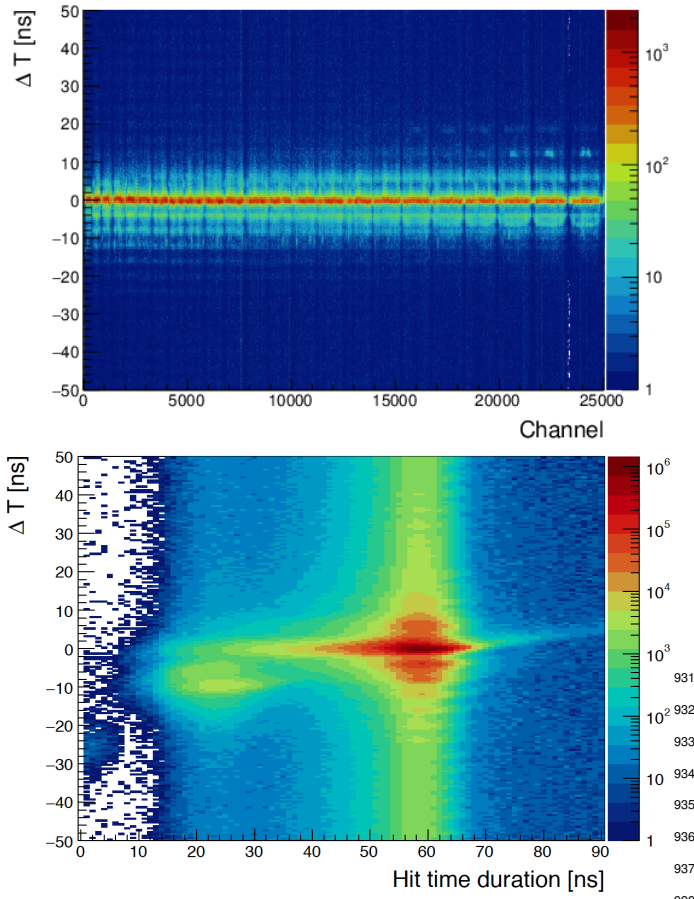


Figure 40: Distribution of the time difference ΔT between the measured RICH and extrapolated CLAS12 times after the time calibration. On the top as a function of the readout channel; on the bottom as a function of the signal amplitude ToT.

the left. The ray-tracing approach allows, for each particle hypothesis, to anticipate the expected photon pattern and the associated hits on the photodetectors, indicated by the small dots in the figures. The measured RICH hits are shown as open circles, whereas the reconstructed photon hits are shown as the full symbols. Direct and reflected photons are indicated in magenta circles and blue squares, respectively. A remarkable feature of the RICH detector is the low level of spurious hits from accidentals, in-time background (i.e. Rayleigh scattering), and dark counts. This feature is crucial for the most challenging cases: particles with high momenta close to the 8 GeV/c limit that require the best resolution in Cherenkov angle, and particles pointing towards the spherical mirror whose number of detected photons is limited by the double reflection and a second passage through the radiator.

For each event, the details of the time and Cherenkov angle reconstruction are shown on the right. On the top panel, the time coincidence ΔT between the RICH measured hit and the CLAS12 calculated time is displayed as a function of the photon flight time within the RICH (photon transit time). The time coincidence ΔT should be close to zero for any true photon path. As a consequence, a valid photon reconstruction

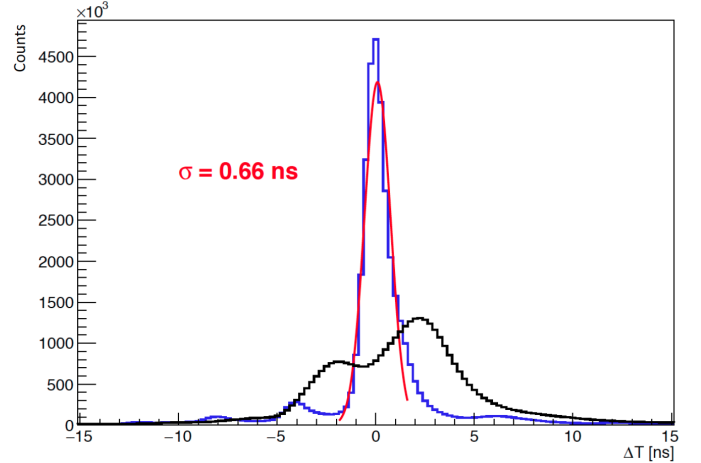


Figure 41: Typical ΔT distribution before (black) and after (blue) the time-walk correction for all RICH pixels. The red line is a Gaussian fit of the corrected distribution, with a global width $\sigma=0.66$ ns

is initially selected by requiring $\Delta T < 3$ ns, indicated by the horizontal dashed lines. The photon path length is represented by the transit time inside the RICH, from the emission point within the aerogel to the detection point in the MaPMT plane after all possible reflections. Photons reflected by the spherical mirror and directed back to the aerogel travel twice the gap, with an expected significant increase of path length and a corresponding distinctive ≈ 6 ns longer transit time.

In the bottom panel, the measured angles are compared to the expected distributions for different particle hypotheses. The width of each distribution corresponds to the expected SPE angular resolution, while the average value depends on the particle type and momentum. An acceptance range is defined from the smallest angle expected for a proton to the largest angle expected for an electron, enlarged by three times the expected angular resolution. For the latter, a conservative value of 6 mrad is taken for the single photon case. These limits are indicated by the vertical dashed lines.

For each reconstructed photon path an estimate of the corresponding Cherenkov angle is obtained and histogrammed on the plot. In all cases studied, both reflected and direct photon information is consistent with the electron hypothesis. In particular, the reconstructed reflected and direct photon paths with ΔT close to zero provide Cherenkov angle values consistent with an electron, as expected. The narrow distribution of the measured angle values indicate that kaons can clearly be separated up to momenta greater than 6 GeV/c. Electrons can be distinguished from pions only at low momenta, below 2 GeV/c.

Each aerogel tile presents specific features because the challenging production process, tuned to achieve the highest transparency over a large volume, is not fully industrialized. The most important quality parameters are the density, related to the average refractive index, homogeneity, related to the refractive index variations within the volume, and tile bending, originated by the inner material tension and related to the

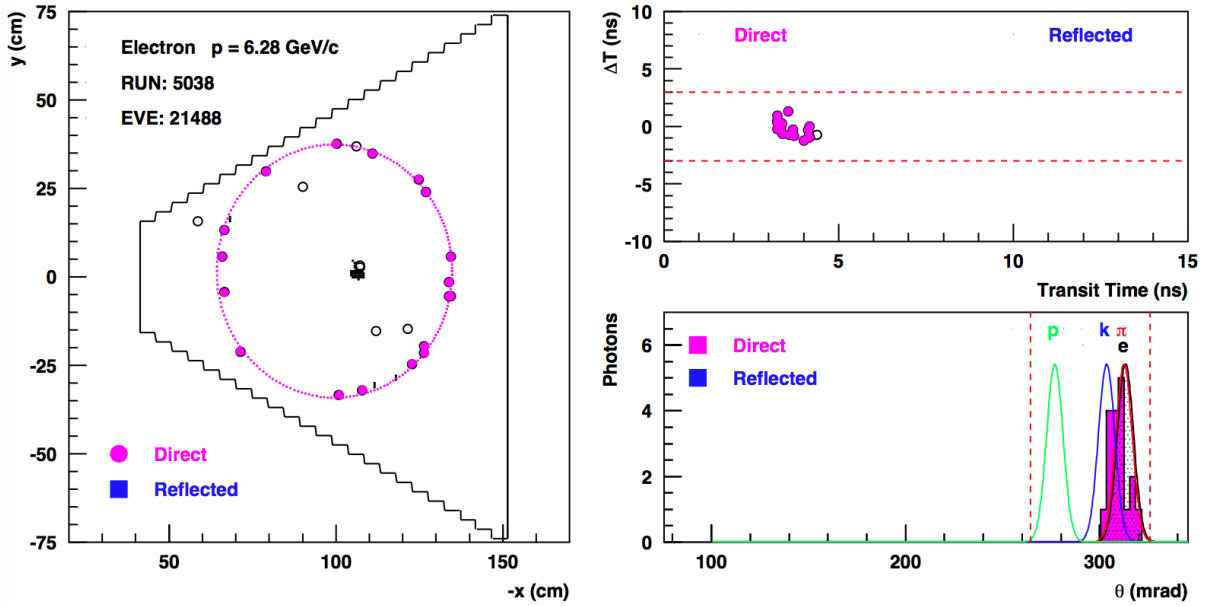


Figure 42: Example of a reconstructed RICH event with only direct photons. On the left the event display, on the right the time (top) and angle (bottom) analysis. Refer to the text for details.

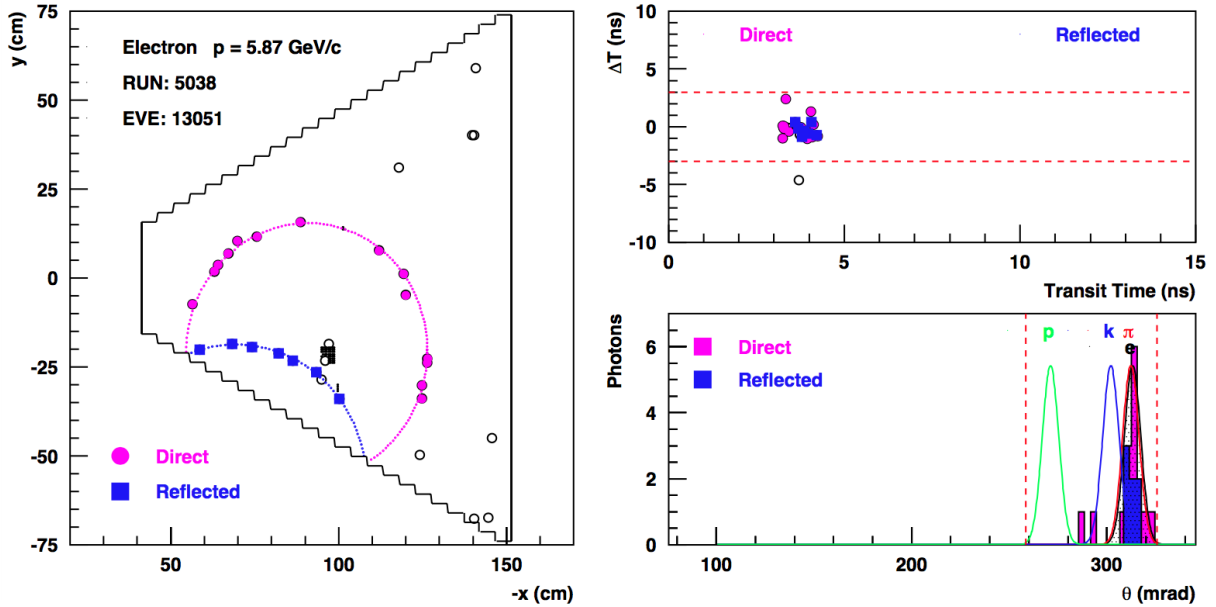


Figure 43: Example of a reconstructed RICH event with a partial ring reflected by the lateral flat mirror. On the left the event display, on the right the time (top) and angle (bottom) analysis. Refer to the text for details.

surface planarity. The effect of these features on the RICH₉₇₆ photon reconstruction can be studied in detail using the control₉₇₇ sample of electrons identified by CLAS12. Given the large₉₇₈ number of tiles and the broad range of particle directions after₉₇₉ the CLAS12 bending magnets, such a study requires large₉₈₀ statistics and is still ongoing. A similar approach is used for the₉₈₁ alignment study. Also in this case, large statistics are needed₉₈₂ due to the numerous involved components (aerogel layers,₉₈₃ mirrors, and MaPMT plane) and photon path configurations.₉₈₄

As a general approach, the RICH performance is studied separately for each aerogel tile. The RICH global performance estimators are then defined by averaging the results over all the radiator tiles. Despite the fact that the above studies have not yet been finalized, and only partial corrections have been implemented so far, the preliminary SPE Cherenkov angle resolution yields typical values around 6 mrad. It is expected to improve towards the goal value of 4.5 mrad once the corrections for the detector misalignment are implemented and the realistic

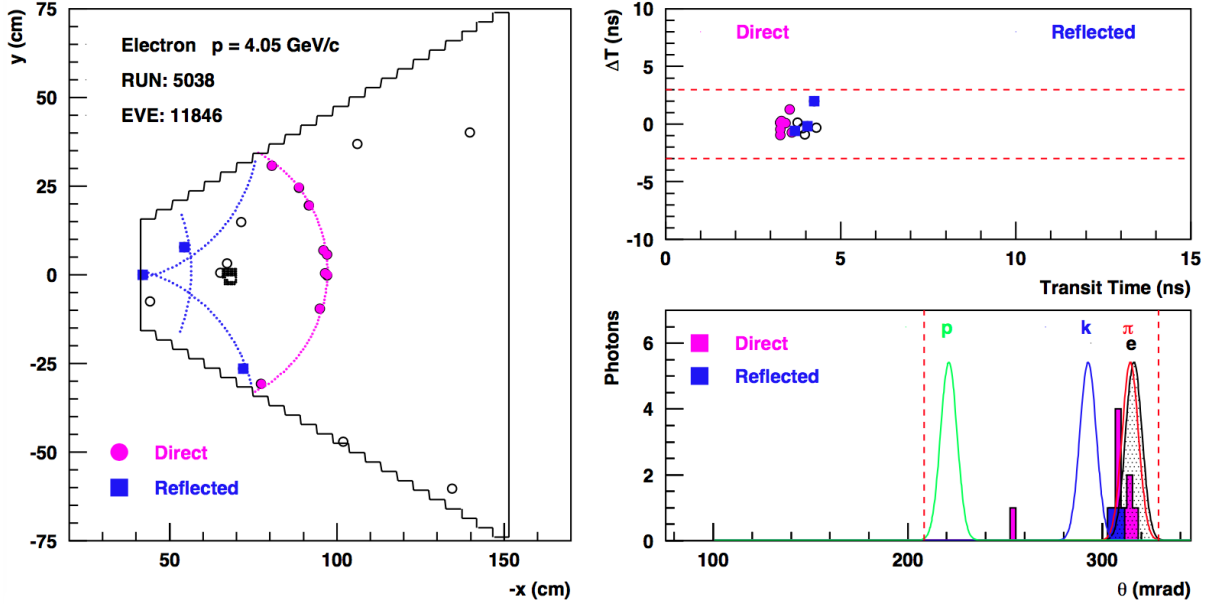


Figure 44: Example of a reconstructed RICH event with photons reflected by all the lateral mirrors. On the left the event display, on the right the time (top) and angle (bottom) analysis. Refer to the text for details.

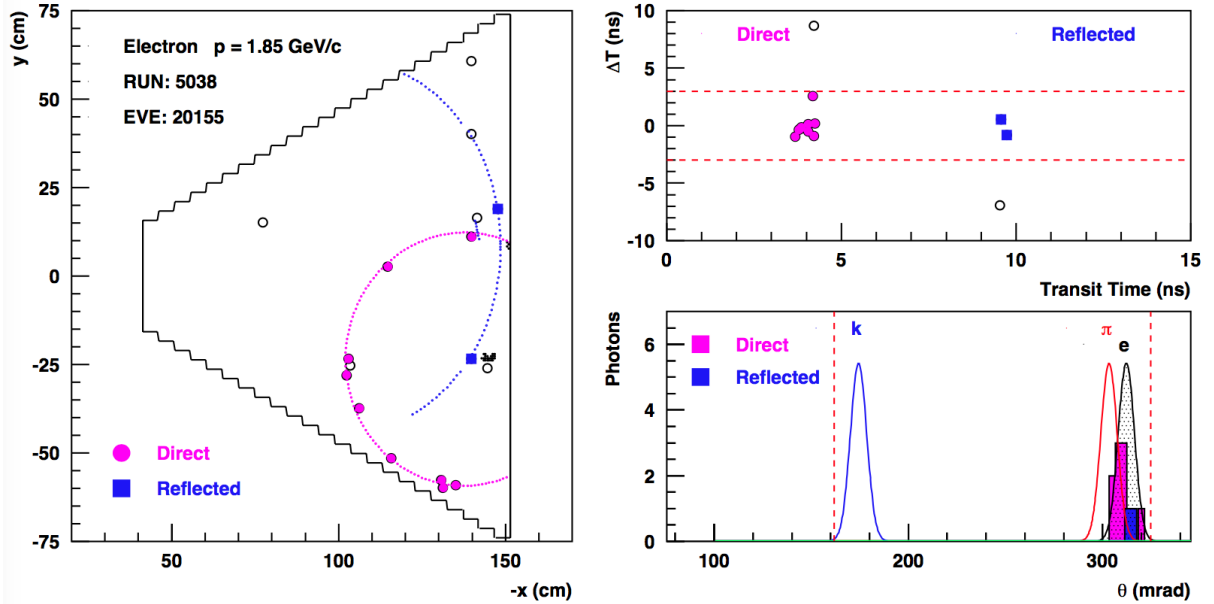


Figure 45: Example of a reconstructed RICH event with a partial ring reflected back by the spherical mirror and passing twice the aerogel layer. On the left the event display, on the right the time (top) and angle (bottom) analysis. Refer to the text for details.

985 optical parameters of each aerogel tile are taken into account.

As an example, the effect of a preliminary alignment of the RICH as a whole is shown for one aerogel tile in Fig. 46. The resolution is calculated as the RMS of the distribution of the average Cherenkov angles extracted for each single track of the⁹⁸⁶ electron control sample. Such averages are calculated over the⁹⁸⁷ detected photons, whose reconstructed path satisfies the time⁹⁸⁸ coincidence and provides an angle within the kinematic limits⁹⁸⁹ described above, associated with the track. The fit shown uses⁹⁹⁰

the function

$$\sigma = \sqrt{\frac{\sigma_1^2}{N} + \sigma_0^2}$$

to extract the single photon resolution σ_1 in addition to a constant term σ_0 measuring the residual systematics due, e.g. to misalignment. After (a preliminary) alignment, the resolution improves toward the design values, which are 4.5 mrad for single photon detection and 1.5 mrad for the average over all the

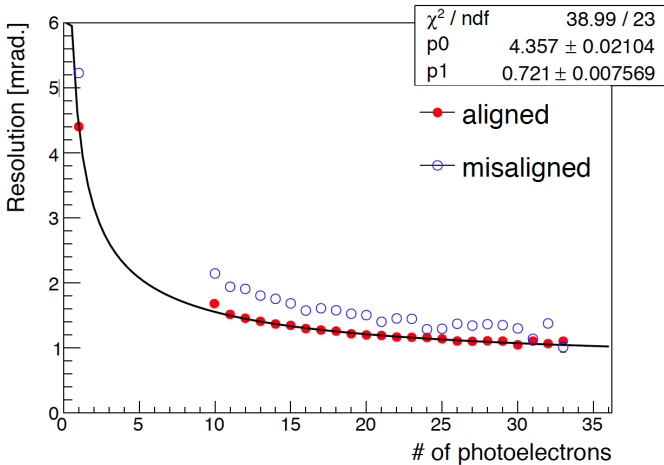


Figure 46: RICH Cherenkov resolution before (open points) and after (solid points) a preliminary RICH alignment. The whole RICH detector is aligned minimizing the matching distance between the RICH clusters and the extrapolated drift chamber tracks. No possible misalignment of a single RICH component is accounted for. The distribution is for particles passing through one aerogel tile of 2-cm thickness (tile 12 in layer 1) and for direct photons.

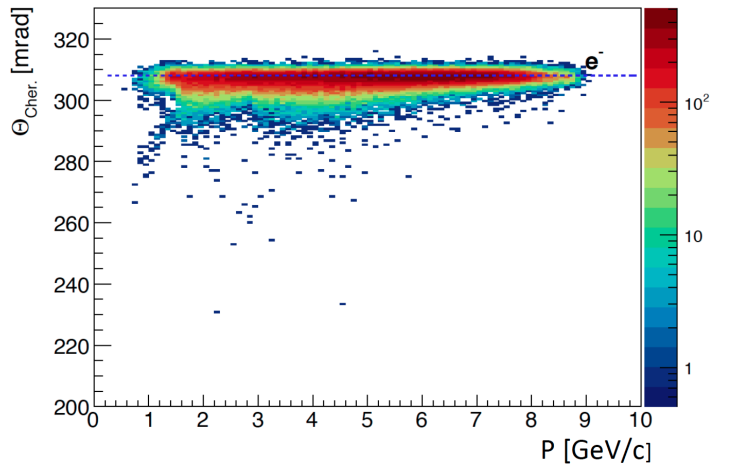


Figure 47: RICH response for electrons as identified by CLAS12. As expected, the measured Cherenkov angle is saturated over the whole momentum range, from 3 GeV/c up to 8 GeV/c. The distribution is for particles passing through one aerogel tile of 2-cm thickness (tile 12 in layer 1) and direct photons.

photons that are associated with the control electron track. As it is shown in Figs. 47 to 49, the preliminary Cherenkov angle resolution is sufficient for hadron separation in the required momentum range from 3 GeV/c to 8 GeV/c. As expected for electron particles identified in CLAS12 by the gas Cherenkov counter HTCC and the calorimeter, the RICH reconstructed Cherenkov angle is saturated to the maximum value in the whole momentum range, see Figs. 47. For positive particles not identified as positrons by other detectors, the RICH measured Cherenkov angles concentrate around the expected values for pion, kaon, and proton particles depending on their momentum, see Fig. 48. The three hadron populations are separated over the whole momentum range, see Fig. 49.

6. Conclusions

A RICH detector has been designed to enhance the hadron identification capability at CLAS12 in the 3 GeV/c to 8 GeV/c momentum range. It substitutes the baseline LTCC gas threshold Cherenkov detector in two of the CLAS12 sectors to create a symmetric left-right setup optimized for running with polarized targets. The first module was installed at the beginning of 2018, in time for the start of the experiment data taking. The second module is under construction and expected to be ready in the summer 2021, in time for the first run with polarized targets.

To efficiently cover the desired momentum range, the RICH employs innovative technological solutions. Among these are composite aeronautic light-materials to ensure the needed mechanical structure rigidity, aerogel radiators of unprecedented large volume (up to $200 \times 200 \times 30$ mm³) and high transparency (≈ 50 mm scattering length), light mirrors (of the order of 1% radiation length) made of carbon fiber or, for the first time in a nuclear experiment, glass-skin technology, and

highly segmented and highly packed Hamamatsu H8500 and H12700 multi-anode photomultipliers. A compact and scalable readout electronics system has been realized for the detector, able to discriminate Cherenkov signals down to as small as a 1/32 fraction of the single photon amplitude, with excellent efficiency and stability, and a time resolution better than 1 ns.

The peculiar geometry of the CLAS12 sector suggested an innovative hybrid-optics solution to limit the active area to ≈ 1 m² per sector, with part of the light directly imaged and part of the light detected after reflection from mirrors. This and the bending into the torus field of the CLAS12 Forward Detector create a variety of possible topologies for the particle and photons paths. The RICH reconstruction exploits a ray-tracing algorithm to provide a Cherenkov angle estimation for each photon hit and hadron track in the event. This basic experimental information allows an independent development of higher-level PID algorithms with increasing sophistication.

Preliminary data analysis shows that the CLAS12 RICH is able to match the required time and Cherenkov angle resolutions. After calibration, each of the 25k channels features a time resolution of the order of 0.6 ns, better than the 1 ns specification. High-momentum particles define the most stringent requirements for the RICH performance. As the pion yield is larger than the other particles species by an order of magnitude, a 4σ angle separation is required to contain the contamination at the percent level. At 8 GeV/c, this implies an angle resolution of 1.5 mrad. Despite the fact that the detailed study of the alignment and optical performance of the various components is still ongoing, the detector has already demonstrated a single-photon angle resolution better than 5 mrad and an average number of 19 photons per charged particle in the forward high-momentum direction, in line with the detector design specifications. This reflects in an angle resolution per charged particle close to the design value of 1.5 mrad and an effective hadron identification capability over

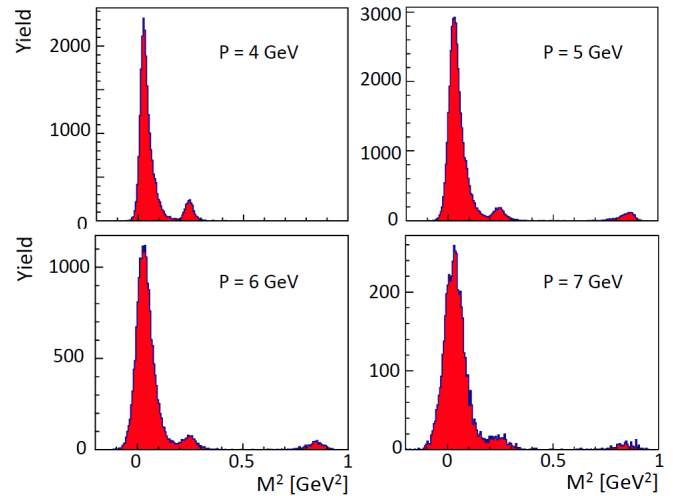
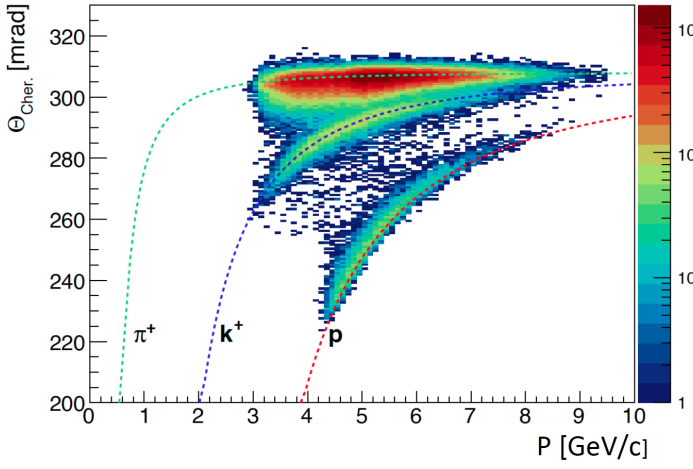


Figure 48: RICH response for non-electron particles as defined by CLAS12. The measured Cherenkov angles distribute around the expected values for pion, kaon, and proton hypotheses as a function of their momentum. The three hadron populations are separated over the whole momentum range, from 3 GeV/c up to 8 GeV/c. The distribution is for particles passing through one aerogel tile of 2-cm thickness (tile 12 in layer 1) and spanning the entire momentum range of interest for RICH.

1058 the entire required momentum range.

1059 7. Acknowledgments

1060 This material is based upon work supported by INFN under¹⁰⁰
 1061 the MIUR priority project CLASMED, Italy and by the U.S.¹⁰¹
 1062 Department of Energy, Office of Science, Office of Nuclear¹⁰²
 1063 Physics under contract DE-AC05-06OR23177 and the National¹⁰³
 1064 Science Foundation, Award #1615067. We thank the JLab¹⁰⁵
 1065 Detector Support Group and Fast Electronics Group, the Hall B¹⁰⁶
 1066 technical and management staff, and the INFN technical and¹⁰⁷
 1067 administrative service.

1068 References

- [1] Y. Sharabian *et al.*, “The CLAS12 High Threshold Cherenkov Counter”, to be published in Nucl. Inst. and Meth. A, (2020). (see this issue)
- [2] M. Ungaro *et al.*, “The CLAS12 Low Threshold Cherenkov Counter”, to be published in Nucl. Inst. and Meth. A, (2020). (see this issue)
- [3] D.S. Carman *et al.*, “The CLAS12 Forward Time-of-Flight System”, to be published in Nucl. Inst. and Meth. A, (2020). (see this issue)
- [4] V.D. Burkert *et al.*, “The CLAS12 Spectrometer at Jefferson Laboratory”, to be published in Nucl. Inst. and Meth. A, (2020). (see this issue)
- [5] G. Asryan *et al.*, “The CLAS12 Forward Electromagnetic Calorimeter”, to be published in Nucl. Inst. and Meth. A, (2020). (see this issue)
- [6] M. Contalbrigo *et al.*, “The Large-Area Hybrid-optics CLAS12 RICH Detector: Tests of Innovative Components”, Nucl. Inst. Meth. **A766**, 22 (2014).
- [7] M. Contalbrigo *et al.*, “Aerogel mass production for the CLAS12 RICH: Novel characterization methods and optical performance”, Nucl. Inst. Meth. **A876**, 168 (2017).
- [8] E. Aschenauer *et al.*, “Optical Characterization of $n = 1.03$ Silica Aerogel used as Radiator in the RICH of HERMES”, Nucl. Inst. Meth. **A440**, 338 (2000).
- [9] <http://www.compositemmirrors.com/>.
- [10] G.J. Barber *et al.*, “Development of Lightweight Carbon-Fiber Mirrors for the RICH 1 Detector of LHCb”, Nucl. Inst. Meth. **A593**, 624 (2008).
- [11] C D'Ambrosio *et al.*, “Precision optical systems for the new generation of Ring Imaging Cherenkov detectors in high energy physics experiments.”, Nucl. Inst. Meth. **A478**, 344 (2002).
- [12] <https://www.evaporatedcoatings.com/>.
- [13] <http://www.media-lario.com/>.
- [14] https://www.hamamatsu.com/resources/pdf/etd/H8500_H10966 TPMH1327E.pdf.
- [15] R. A. Montgomery *et al.*, “Multianode Photomultiplier Tube Studies for Imaging Applications”, Nucl. Inst. Meth. **A 695**, 326 (2012).
- [16] S. Anefalos Pereira *et al.*, “Test of the CLAS12 RICH Large Scale Prototype in the Direct Proximity Focusing Configuration”, Eur. Phys. J. A **52**, 23 (2016).
- [17] <https://www.hamamatsu.com/resources/pdf/etd/H12700 TPMH1348E.pdf>.
- [18] M. Contalbrigo *et al.*, “Single Photon Detection with the Multi-anode CLAS12 RICH Detector”, Nucl. Inst. Meth. **A 952**, 16123 (2020).
- [19] S. Blin *et al.*, “MAROC, a Generic Photomultiplier Readout Chip”, IEEE Nucl. Sci. Symp. Conf. Rec. 2010, 1690 (2010).
- [20] S. Boyarinov *et al.*, “The CLAS12 Data Acquisition System”, to be published in Nucl. Inst. and Meth. A, (2020). (see this issue)
- [21] Pavel Degtarenko, “Precision Analysis of the Photomultiplier Response to Ultra Low Signals”, Nucl. Inst. Meth. **A872**, 1 (2017).
- [22] P. Degtarenko, V. Kubarovskiy, A. Kim, and A. Smith, to be published.
- [23] Experimental Industrial Physics Control System, <https://epics-controls.org>
- [24] https://www.jlab.org/div_dept/physics_division/dsg/notes/2016-012%20National%20Instruments%20compactRIO-based%20control,%20monitoring,%20and%20interlock%20system.pdf
- [25] M.D. Mestayer *et al.*, “The CLAS12 Drift Chamber System”, to be published in Nucl. Inst. and Meth. A, (2020). (see this issue)
- [26] V. Ziegler *et al.*, “The CLAS12 Software Framework and Event Reconstruction”, to be published in Nucl. Inst. and Meth. A, (2020). (see this issue)